

A RADIO-SELECTED SAMPLE OF GAMMA RAY BURST AFTERGLOWS

POONAM CHANDRA,¹ & DALE A. FRAIL,²
Submitted to ApJ

ABSTRACT

We present a catalog of radio afterglow observations of gamma-ray bursts (GRBs) over a 14 year period from 1997 to 2011. Our sample of 304 afterglows consists of 2995 flux density measurements (including upper limits) at frequencies between 0.6 GHz and 660 GHz, with the majority of data taken at 8.5 GHz frequency band (1539 measurements). We use this dataset to carry out a statistical analysis of the radio-selected sample. The detection rate of radio afterglows has stayed unchanged almost at 31% before and after the launch of the *Swift* satellite. The canonical long-duration GRB radio light curve at 8.5 GHz peaks at 3-6 days in the source rest frame, with a median peak luminosity of 10^{31} erg s⁻¹ Hz⁻¹. The peak radio luminosities for short-hard bursts, X-ray flashes and the supernova-GRB classes are an order of magnitude or more fainter than this value. There are clear relationships between the detectability of a radio afterglow and the fluence or energy of a GRB, and the X-ray or optical brightness of the afterglow. However, we find few significant correlations between these same GRB and afterglow properties and the peak radio flux density. We also produce synthetic light curves at centimeter and millimeter bands using a range of blastwave and microphysics parameters derived from multiwavelength afterglow modeling, and we use them to compare to the radio sample. Finding agreement, we extrapolate this behavior to predict the centimeter and millimeter behavior of GRBs observed by the Expanded Very Large Array (EVLA) and the Atacama Large Millimeter Array (ALMA).

Subject headings: gamma rays: bursts—cosmology: observations—hydrodynamics—radio continuum: general

1. INTRODUCTION

Our understanding of gamma-ray bursts (GRBs) has advanced rapidly since the discovery of the long-lived “afterglows” at X-ray, optical and radio wavelengths (Costa et al. 1997; van Paradijs et al. 1997; Frail et al. 1997). Since that time many more γ -ray and hard X-ray satellites have monitored the sky for GRBs providing accurate localizations and enabling detailed followed up by the space and ground-based facilities at longer wavelengths. As a result of this large and sustained effort, several hundred afterglows have been detected over the last 15 years. The afterglow study has exposed a rich diversity of GRB behaviors and several distinct progenitor classes (Gehrels et al. 2009). While many of the early advances in the field were the result of studying individual GRBs and their afterglows, the field has now matured to the point where much more can be learned from the study of large samples.

Statistical analysis have long been carried out on GRB-only samples (e.g. Kouveliotou et al. 1993; Sakamoto et al. 2011) but including afterglow data has only been done recently. Compilations of X-ray and optical light curves from the *Swift* satellite have revealed complex but canonical light curve behaviors (Nousek et al. 2006; Zhang et al. 2006; Melandri et al. 2008; Roming et al. 2009; Evans et al. 2009). Optical catalogs have derived mean dust extinction laws of GRB host galaxies (Kann et al. 2006; Starling et al. 2007), and have lead to claims of clustering of the optical af-

terglow luminosities (Liang & Zhang 2006; Kann et al. 2006; Nardini et al. 2006).

Comparative studies of GRBs and their afterglows have proven even more useful. The standard fireball model has been tested through spectral and temporal comparisons of X-ray and optical light curves (e.g. Oates et al. 2009, 2011; Schulze et al. 2011). Significant differences have been found between the mean brightness and the redshift distribution of the *Swift* and the pre-*Swift* GRBs (Berger et al. 2005b; Jakobsson et al. 2006; Kann et al. 2010). Correlations have been found for both short and long-duration bursts between the gamma-ray fluence and the X-ray and optical afterglow brightness (Gehrels et al. 2008; Nysewander et al. 2009; Kann et al. 2011). A population of dark bursts has been identified (Rol et al. 2005), as has a population of nearby, low luminosity events (Sazonov et al. 2004; Soderberg et al. 2006a; Pian et al. 2006; Liang et al. 2007; Kann et al. 2010).

In comparison, very little effort has gone into compiling radio afterglow data and carrying out correlative studies (Berger 2004a). A catalog of the first five years of radio afterglow data was produced by Frail et al. (2003), but comparisons were limited just between detection rates of X-ray, optical and radio afterglows. The mean flux densities and luminosities of radio afterglows were given in Frail (2005), while Soderberg et al. (2006a) compiled radio light curves to compare GRB and supernova luminosities. Recently de Ugarte Postigo et al. (2011b) has compiled the mm/submm data of GRBs and carried out the cumulative analysis in view of upcoming Atacama Large Millimeter Array (ALMA). Since the launch of the *Swift* satellite the number of GRBs with radio data

¹ Department of Physics, Royal Military College of Canada, Kingston, ON K7M3C9, Canada; Poonam.Chandra@rmc.ca

² National Radio Astronomy Observatory, 1003 Lopezville Road, Socorro, NM 87801.

has doubled. Moreover, in the near future the continuum sensitivity of the Very Large Array³ (VLA; now Expanded Very Large Array) - the primary telescope for radio afterglow follow-up - will increase by a factor of 5 to 20 (depending on wavelength). It is therefore timely to pull together all the past radio data in one place and to use the catalog to define the average properties of radio afterglows, search for trends in different sub-classes of GRBs (e.g. short vs long), search for differences in the *Swift* and pre-*Swift* sample, and to investigate if there are any correlations between the radio afterglows and the prompt or afterglow emission at shorter wavelengths.

In §2, we present a summary of our radio sample and its properties. We also compare the detection statistics with respect to other wave bands. We discuss the details and statistics of detection versus upper limits of our sample in §3. In §4 and §5, we investigate the distribution and correlative properties of our radio sample with respect to the GRB prompt emission properties as well as the X-ray and optical afterglow properties. We plot the synthetic radio light curves and their dependence on various parameters in §6. We use these light curves to make some predictions for the Atacama Large Millimeter Array (ALMA) in §7, while in §8 we bring together to summarize the various results of the paper.

We adopt a Λ -CDM cosmology throughout this paper with $H_0 = 71 \text{ km s}^{-1} \text{ Mpc}^{-1}$, $\Omega_m = 0.27$ and $\Omega_\Lambda = 0.73$ (Spergel et al. 2007).

2. THE RADIO SAMPLE AND STATISTICS

2.1. Radio Sample

Our compiled sample consists of 304 GRBs observed with the radio telescopes between January 1997 and January 2011, along with the 2011 April 28 Fermi burst, GRB 110428A. The sample consists of a total of 2995 flux density measurements taken between the frequencies 0.6 GHz to 660 GHz bands spanning a time range from 0.026 to 1339 days. In Figure 1, we plot the histogram summarizing the distribution of the data in our catalog, as a function of frequency and time elapsed since the burst. A total of 1539 measurements were taken in 8.5 GHz frequency band, while 657 measurements were taken in 5 GHz frequency band.

The sample includes 33 Short-hard bursts (SHBs), 19 X-ray flashes (XRFs) and 26 GRBs with possible supernova associations (SN/GRBs). The SN/GRB category includes all the GRBs with confirmed associations as well as likely supernova (SN) associations (see Hjorth & Bloom 2011). The SN/GRBs with known supernovae (SNe) associated with them in our sample are: GRB 980425 (SN 1998bw), GRB 011121 (SN 2001ke), GRB 021211 (SN 2002lt), GRB 030329 (SN 2003dh), GRB 031203 (SN 2003lw), GRB 050525A (SN 2005nc), GRB 060218 (SN 2006aj), GRB 091127 (SN 2009nz) and GRB 101219B (SN 2010ma). The spectroscopically confirmed SN associations among these are GRBs 980425, 030329, 031203, 060218 and 091127. Of the 26 SN/GRBs associations, 17 and 9 were discovered in the pre-*Swift* and post-*Swift* epoch, respectively. Among the 33 SHBs,

³ The Very Large Array is operated by the National Radio Astronomy Observatory, a facility of the National Science Foundation operated under cooperative agreement by Associated Universities, Inc.

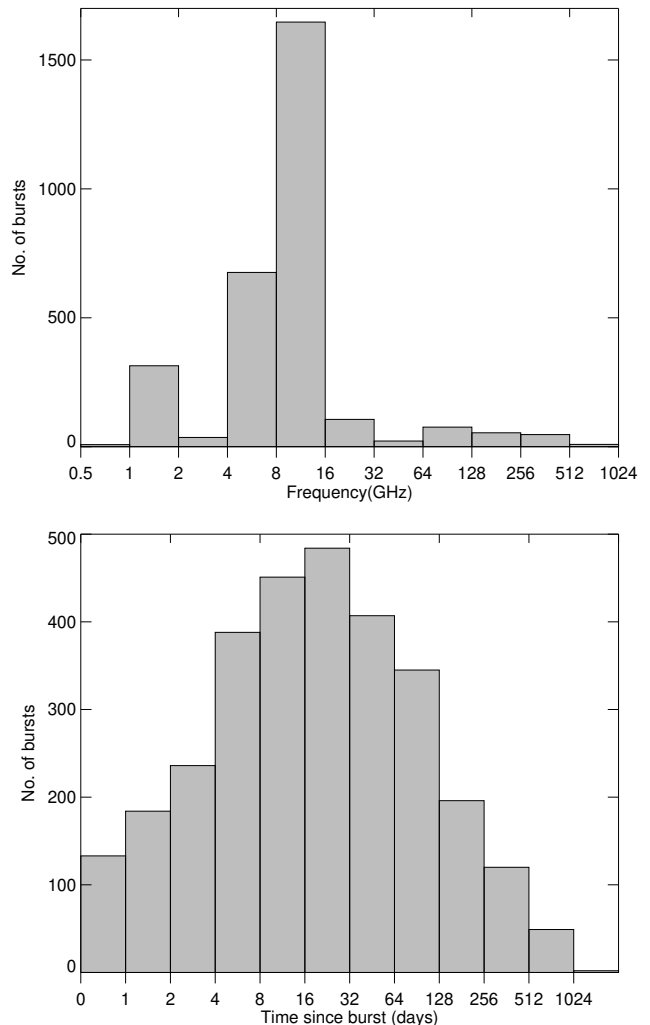


Figure 1. Histograms summarizing the distribution of data of the radio selected sample catalog as a function of observing frequency (upper panel) and of the time elapsed since the burst (lower panel).

28 were detected by the *Swift* alone. We also have one candidate galactic transient in our sample (GRB 070610, Kasliwal et al. 2008; Castro-Tirado et al. 2008).

Most of the afterglows (270 in total) in our sample were observed as part of the VLA radio afterglow programs, whereas, 15 bursts were observed by the Expanded VLA (EVLA), and 19 southern bursts with the Australia Telescope Compact Array (ATCA). Among the total of 285 VLA/EVLA bursts, 8 bursts were followed by both the VLA/EVLA and the ATCA; and 38 bursts were observed by the Westerbork Synthesis Radio Telescope (WSRT) in addition to the VLA/EVLA. A total of 19 VLA/EVLA bursts were followed by the Ryle telescope, and 11 bursts in our sample were observed by the Giant Metrewave Radio Telescope (GMRT). The Very Long Baseline Array (VLBA) with its sub-milliarcsecond angular resolution was used to observe five bursts (see Table 6).

For the VLA observations, most of the afterglows were first observed in the 8.5 GHz frequency band, since it is the most sensitive VLA band. Once a GRB was detected in the 8.5 GHz band, we followed it at other VLA frequencies to measure the continuum spectrum. However, in cases of bright, nearby or high-redshift (high- z) GRBs

or GRBs with good amount of multiwaveband data, we carried out follow-up observations for few epochs even for the initially non-detected afterglows, depending upon its interest in other wavebands, VLA time availability factors etc. The data were taken in standard interferometric mode for an integration time of typically 30 minutes (including the time on the calibrators and the GRB integration time). The total bandwidth used was 100 MHz. The data was analysed using standard *AIPS* routines.

In Table 6, we list the comprehensive properties of our sample. In column 1, the GRB names are given. Column 2 lists the missions under which these GRBs were discovered (please refer to the table notes for the abbreviations of the mission names). We tabulate the J2000 positions of the GRBs in columns 3 and 4. Columns 5, 6 and 7 tabulate the detection statistics in X-ray, optical and radio bands, respectively. Symbol ‘Y’ indicates a detection, while ‘N’ indicates a non-detection. The symbol ‘X’ means the burst was not observed in that particular band, whereas ‘Y?’ indicates that the observation was made but a detection could not be confirmed. Column 8 tabulates all the radio telescopes used to observe the corresponding burst. We report the T_{90} durations (the time interval over which 90% of the total background subtracted counts are observed, with the interval starting at 5% of the total counts have been observed (Koshut et al. 1995)) in the observer’s frame and the redshifts z in columns 9 and 10, respectively. Here T_{90} durations are mentioned in the energy band of the specific detector which detected a GRB. For example, for *Swift* bursts, the T_{90} durations are in 15–350 keV energy range. Column 11 shows the 15–150 keV fluences (S_{15-150}) of our sample and column 12 indicates the k -corrected isotropic bolometric γ -ray energy (E_{iso}^{bol} , energy range 1–10,000 keV in the rest frame). We report the X-ray fluxes at 11 hr (F_X^{11h}) in 0.3–10 keV range in column 13. Here the fluxes for the *BeppoSAX* bursts are quoted in 1.6–10 keV range. We also report the R-band (0.7 μ m) optical flux densities at 11 hr (F_R^{11h} , in μ Jy) in column 14. Column 15 tabulates the jet break times t_j in cases where a clear jet break was seen and column 16 indicates the number density (n) of the circumburst medium. For the GRBs in which the number density of the medium was not known, we have assumed a density of 1 cm^{-3} and have indicated them with “[1]”. We estimate the collimation angle θ_j (degrees) and the beaming-corrected bolometric energy (E_{true}^{bol}) of GRBs with observed t_j using Frail et al. (2001); Bloom et al. (2003) and tabulate them in columns 17 and 18, respectively. Column 19 lists the references. Each cell has 8 references in the following order: T_{90} , z , S_{15-150} , E_{iso}^{bol} , F_X^{11h} , F_R^{11h} , t_j , and n . If there is no data in a particular cell, the corresponding reference is indicated with []. However, a reference indicated by [] for a non-empty corresponding cell implies that that particular value has been calculated by us and this paper is the reference.

2.2. Multiwaveband detection statistics of our sample

In Table 1, we summarize the detection statistics in radio, X-ray and optical bands for all the bursts in our sample. We subdivide the sample into pre-*Swift* and post-*Swift* bursts. This split was made to investigate possible selection biases. The pre-*Swift* GRB event rate was low

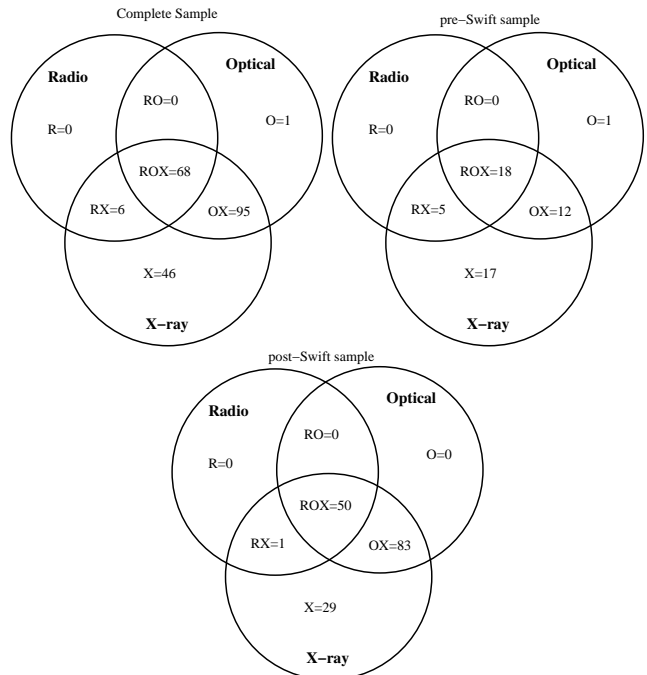


Figure 2. Venn diagrams illustrating the different relationships between the radio, optical, and X-ray afterglows for the entire sample, the pre-*Swift* and the post-*Swift* sample. The symbols X, O and R indicates detections in X-ray, optical and radio bands, respectively. The combinations of these letters indicate detections in those respective bands. For example, RX indicates detection in radio and X-ray but not in optical, while ROX indicate afterglows seen in all three bands.

enough that radio follow-up was undertaken for nearly all events (see Frail et al. 2003), while only a subset could be observed among the *Swift* bursts.

Out of the 304 bursts, 123 bursts were observed in the pre-*Swift* epoch from 1997 until 2004. The remaining 181 bursts were observed between 2005 and April 2011. A total of 95 bursts resulted in radio detections, while 206 were non-detections. For three bursts an initial detection could not be confirmed. Thus the total detection rate for our sample in the radio band is 31%. The radio detection statistics in pre-*Swift* and post-*Swift* samples are 42/123 (34%) and 53/181 (29%), respectively. It is striking how similar the detection ratios are in both samples. In contrast, the X-ray detection rates increase from 42% to 93% after the launch of *Swift*. This is because of the dedicated X-ray telescope (XRT) on-board *Swift*, which autonomously slewed to Burst Alert Transient (BAT; onboard *Swift*) detected bursts. Note also that 51% of the bursts were not observed in the X-ray bands in the pre-*Swift* sample. The optical detection rates also increased from 48% to 75% between the pre-*Swift* and the post-*Swift* epoch. This too was due to the on-board UV/optical telescope (UVOT) which was autonomously slewed along with the XRT, and also due to the availability of rapid, well-localized positions for ground-based follow-up. We refer the reader to Table 1 for the detailed statistics of the multiwaveband observations of our sample.

In Figure 2, we plot a Venn diagram for our entire sample illustrating the different relationships between the radio, optical and X-ray observations of the afterglows. We also indicate this relationship for the pre-*Swift* and the

Table 1
Multiwaveband statistics of the GRB afterglow sample

	Complete sample						Pre- <i>Swift</i> sample						Post- <i>Swift</i> sample					
	Radio		Optical		X-ray		Radio		Optical		X-ray		Radio		Optical		X-ray	
	No.	frac.	No.	frac.	No.	frac.	No.	frac.	No.	frac.	No.	frac.	No.	frac.	No.	frac.	No.	frac.
Detection	95	0.31	196	0.65	221	0.73	42	0.34	60	0.49	52	0.42	53	0.29	136	0.75	169	0.93
Non-detection	206	0.68	94	0.32	13	0.05	81	0.66	55	0.45	6	0.05	125	0.69	39	0.22	7	0.04
Not-observed	0	0	10	0.03	68	0.23	0	0	8	0.06	63	0.51	0	0	2	0.01	5	0.03
Unconfirmed	3	0.01	4	0.02	2	0.01	0	0	0	0	2	0.02	3	0.02	4	0.02	0	0
Total	304	1	304	1	304	1	123	1	123	1	123	1	181	1	181	1	181	1

post-*Swift* sample separately. For the Venn diagrams, if a GRB did not have an observation in any band (i.e. 'X' in Table 1), we excluded them. We also excluded those events which had a unconfirmed detection in any bands (i.e. 'Y?'). Thus, we included a total of 226 bursts, out of which 10 bursts had no detection in any band. Among those 10 bursts with no afterglow detection, 6 are SHBs (GRBs 021201, 020531, 050911, 051105A, 071112B and 090417A) and the remaining are normal long GRBs (GRBs 970111, 990217, 000615A and 071018). Hence, the final Venn diagram of the complete sample includes 216 bursts. The X-ray detections are marked with X, optical detections are marked with O and radio detections are marked with R. ROX indicates the bursts which were detected in all three bands, whereas a combination of two letters indicates a joint detection in those respective wavelengths. For example, RX indicates bursts detected in radio and X-ray bands but not in optical. A single letter, X for example, indicates an afterglow detected in the X-ray band only. Our sample consists of 68 bursts which were detected in all three bands. There were 95 bursts which had detections in X-ray and optical but not in radio. There was no burst which was detected in only the radio band (i.e. R), nor were there any bursts detected in only the radio and the optical bands without being detected in the X-ray band (i.e. RO). However, 6 bursts were detected in the radio and the X-ray bands but not in the optical. These form a subset of the dark bursts. Only one optical burst could not be detected in any other band. The number of only X-ray detected afterglows is 46. In the post-*Swift* and the pre-*Swift* samples the X-ray only afterglows are 29 and 17, respectively. In the pre-*Swift* sample the GRBs detected in all three bands was only 18, rising to 50 in the post-*Swift* bursts.

3. RADIO AFTERGLOW SAMPLE ANALYSIS

3.1. Radio flux density distributions

Since our data consists of detections as well as upper limits, we incorporated the Kaplan–Meier Product Limit method (K–M; Feigelson & Nelson 1985) in deriving the flux density distributions and mean flux density estimates of our sample. The K–M estimator was applied to a sample of bursts for which flux density measurements had been made at one frequency over a fixed time interval. For detections, we averaged multiple observations of the same GRB to obtain the mean flux density. This is perfectly acceptable since over the short periods the flux density variations at radio frequencies are dominated by interstellar scintillation. Table 2 summarizes our results for 5 and 8.5 GHz bands. Here, the mean estimates are given for only detections as well as by including the upper

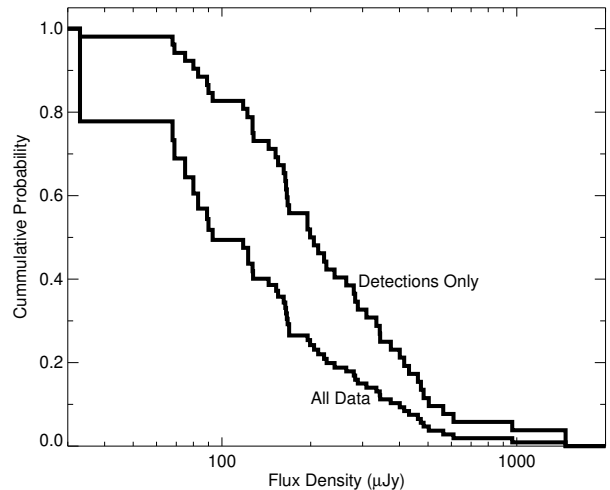


Figure 3. The Kaplan–Meier probability distribution of the radio flux densities at 8.5 GHz for a complete sample of 107 GRBs toward which measurements or upper limits were made between 5 and 10 days. The distribution of the 51 detections is shown for comparison.

limits. The KM_{25} , KM_{50} and KM_{75} are the K–M method estimates of the minimum flux density above which 25%, 50%, and 75 % of the total radio afterglows will lie.

In Figure 3, we plot the Kaplan–Meier probability distribution of the radio flux densities at 8.5 GHz for a complete sample of 107 GRBs toward which measurements or upper limits were made between 5 and 10 days. The distribution of the 51 detections is shown for comparison. The overall detection rate in this time range is 48% (i.e., 51/107). The mean of the 51 detections is $275 \pm 34 \mu\text{Jy}$ while the mean of the entire sample (upper limits included) is $170 \pm 20 \mu\text{Jy}$. Half of all GRBs produce radio afterglows with flux densities at 8.5 GHz in excess of $92 \mu\text{Jy}$.

Before making any detailed comparisons, it is important to understand any possible biases that might exist in these data. Specifically, we ask whether a radio non-detection is the result of an inadequate measurement (i.e., not observing at a correct time or with enough sensitivity), or whether it is the result of an underlying physical cause. In Figure 4, we plot the distributions for the radio 3-sigma upper limits as well as for the detections between 5–10 days. The upper limits peak in 100–150 μJy range, whereas the detections peak in 150–200 μJy range with a tail extending to 1 mJy. As first noted by Frail (2005), the difference in the upper limits and the detections is not highly significant (see also Table 3). There is only about a factor of 50 difference between the radio

Table 2
K–M estimates of the flux density distribution

Freq. GHz	Time range Days	Total Detections	Total Data points	Detections Only				Detections+Upper limits			
				KM ₂₅ ^a μJy	KM ₅₀ ^b μJy	KM ₇₅ ^c μJy	Mean flux μJy	KM ₂₅ ^a μJy	KM ₅₀ ^b μJy	KM ₇₅ ^c μJy	Mean flux μJy
4.86	2 – 8	27	63	362	251	199	290 ± 25	243	155	64	197 ± 17
4.86	5 – 10	17	40	377	248	198	290 ± 35	238	88	44	193 ± 23
4.86	7 – 14	20	39	419	228	152	285 ± 42	237	132	82	206 ± 27
8.46	2 – 8	65	157	389	219	156	287 ± 26	199	107	31	162 ± 15
8.46	5 – 10	51	107	343	197	126	275 ± 34	196	92	55	170 ± 20
8.46	7 – 14	43	99	418	203	123	302 ± 42	185	92	26	173 ± 22

Note. —

^a K–M estimates that 25% of all bursts will have radio afterglows above this value.

^b K–M estimates that 50% of all bursts will have radio afterglows above this value.

^c K–M estimates that 75% of all bursts will have radio afterglows above this value.

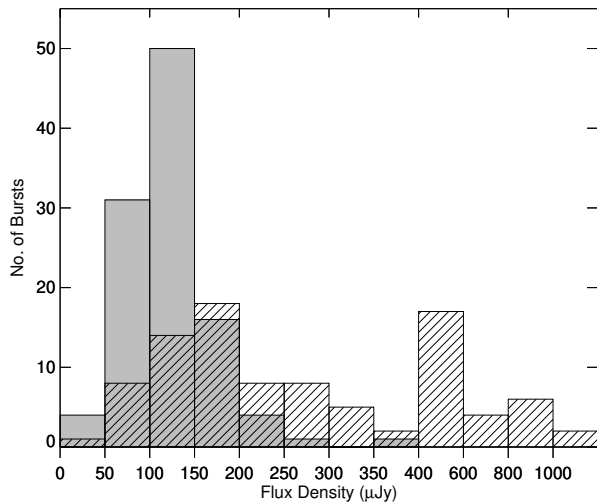


Figure 4. The filled histogram represents the distribution for the 8.5 GHz 3- σ upper limits for GRBs in our sample between days 5–10. The hatched histogram shows the distribution for the detections between days 5–10. The small range of peak flux densities between the radio detections and non-detections suggests that the detection fraction of radio afterglows is largely determined by the instrumental sensitivities.

flux density of the brightest and the faintest detected cosmological bursts (i.e. $z \geq 0.4$). This low dynamic range stands in sharp contrast to the orders of magnitude difference between the bright and faint events seen in either X-ray or afterglow samples (Kann et al. 2006; Racusin et al. 2011). This narrow flux density range suggests that the detection fraction of our radio afterglow sample is determined by the instrumental sensitivities.

In Figure 5, we plot all those GRBs which were never detected in the radio band. We also overlay one rare, bright GRB light curve GRB 980703 (red curve) and a more typical GRB 980329 (blue curve). The plot shows that our upper limits do not cut off at a fixed flux density but are tightly clustered within one order of magnitude (between 30 μJy to around 400 μJy). As illustrated in Figure 5, most of the observations would have been capable of detecting a bright GRB 980703-like afterglow, while up to the first 10 days (when most of the afterglow observations take place), only around 50% observations would have been capable of detecting an average event like GRB 980329. This result reinforces our suggestion that radio afterglow searches are strongly sensitivity lim-

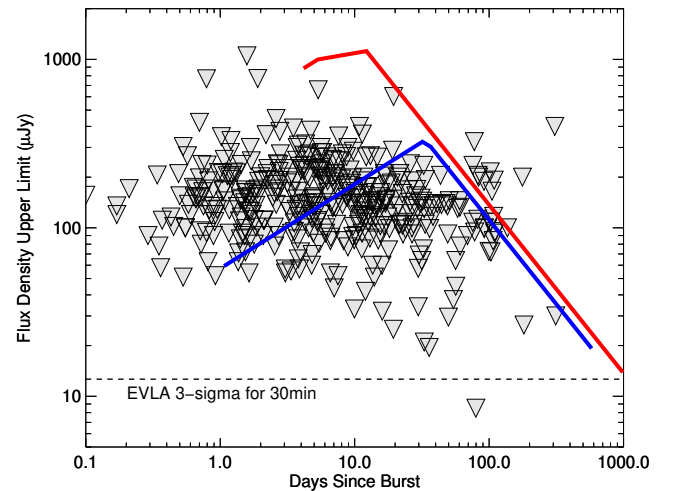


Figure 5. Upper limits at 8.5 GHz frequency band for all GRBs for which no afterglow was detected. The red line represents the light curve of a rare, bright event GRB 980703 and the blue line represents the light curve of a more typical event GRB 980329. The detection fraction of radio afterglows in the first 10 days certainly appears to be mainly limited by the sensitivity. Black dashed line indicates 3-sigma flux density of the EVLA in its full capacity for a 30 min integration time.

ited. In this figure, we also plot the 3-sigma flux density of EVLA for a 30min integration in its full capacity.

3.2. k -corrected radio spectral luminosity

In Figure 6, we plot the k -corrected radio spectral luminosities with the 3-sigma upper limits. To convert the flux density into spectral luminosity L , we use $L = 4\pi F d_L^2 / (1+z)$, where F is the radio flux density and d_L is the luminosity distance corresponding to the redshift z . To incorporate k -correction, we multiply this luminosity with a k -correction factor of $(1+z)^{\alpha-\beta}$ (where α and β are the time and frequency indices in $F \propto t^\alpha \nu^\beta$). Thus the k -corrected radio spectral luminosity is $L = 4\pi F d_L^2 (1+z)^{\alpha-\beta-1}$. Here we choose $\alpha = 0$ and $\beta = 1/3$ corresponding to an optically thin, flat, post-jet-break light curve (Frail et al. 2006). For the GRBs with unknown redshift, we assume the average redshifts of pre-*Swift* and *Swift* bursts, i.e. $\langle z \rangle_{pre} = 1.3$ for the pre-*Swift* bursts and $\langle z \rangle_{post} = 2.0$ for the post-*Swift* bursts (see §4.1). In our sample we have 147 GRBs with known redshifts, while 157 GRBs don't have a measured redshift.

This figure, similar to Figures 4 and 5, also shows that for most of the sample, the difference in the spectral luminosities between the detections and the upper limits is not very significant. The average luminosity for detections is 1.1×10^{31} erg s $^{-1}$ Hz $^{-1}$, whereas, the average luminosity $3\text{-}\sigma$ upper limit for non-detections is 6.4×10^{30} erg s $^{-1}$ Hz $^{-1}$, i.e., the difference between them is not even a factor of two. Figure 6 does show, however, the existence of the low-luminosity events which are several orders of magnitude fainter than the normal cosmological events. We will discuss these populations in more detail in §3.4.

3.3. Canonical light curves of radio afterglows

In Figure 7, we plot light curves of all the detected radio afterglows at 8.5 GHz in their rest frames as well as the observer frame, excluding the GRB sub-classes (SHB, XRF and SNe/GRB) from which the low luminosity events in Figure 6 originate. We average these data to produce a mean light curve for the long-duration, cosmological GRBs (LGRB) along with the 75% confidence bands. A canonical LGRB if observed from beginning to end will have a mean luminosity of $\sim 2 \times 10^{31}$ erg s $^{-1}$ Hz $^{-1}$ until about 3–6 d (10–20 d) in the rest-frame (observer-frame). After this time there is a gradual power-law decay with an index of approximately -1 . The mean light curve shows two peaks (rest frame), one between day 0.1–0.2 and one around day 2, and a dip around day 1. The first peak is not significant since there are too few data points. The peak after day 2 is significant but it is likely the same peak as identified in Figure 9. The dip near day 1 appears real and may signify a transition between two different emission components (reverse shock and forward shock).

3.4. Bursts of different classes

We explore the differences in the luminosity light curves of SHBs, XRFs and SN-GRBs. In Figure 8, we plot the radio luminosity light curves for the different GRB classes in the 8.5 GHz band. The top plot is the light curve for SHBs. Our sample included 35 SHBs but there are only two detections GRB 050724 and GRB 051221A. For 13 SHBs the redshift was not known. We averaged the redshifts of known- z SHBs and assigned this value ($\langle z \rangle = 0.55$) to the unknown- z SHBs. Here we also overlay the mean light curve of LGRBs obtained from the Figure 7. It is clear that SHBs are intrinsically radio dim objects. They are more than an order of magnitude fainter than a LGRB. In the middle frame of Figure 8 we plot the light curves of the 19 XRFs in our sample which includes seven detections. Most XRFs are usually only about a factor of ten fainter than LGRB (red curve). The extreme outlier is GRB 060218, which is 4–5 orders of magnitude dimmer than a typical event. In the bottom frame of Figure 8 we selected only those 9 GRBs for which the known SN associations exist. The SNe/GRBs nearly fully populate this radio luminosity plot. Some SNe/GRBs such as GRB 980425 and GRB 060218 are dim, while others like GRB 030329 are as bright as a typical LGRB.

3.5. Peak of radio afterglow detections

Out of the 95 radio-detected afterglows (see §2.2), 63 had radio light curves (i.e. 3 or more detections in a

single radio band), whereas 32 bursts had less than 3 detections. For the GRBs for which the light curves were available, we determined the peak flux density and the time of the peak at the VLA frequency bands (i.e. 1.4 GHz, 4.9 GHz, 8.5 GHz, 15 GHz and 22.5 GHz bands) by fitting the forward shock formula of the form (Frail 2005).

$$f(t) = \begin{cases} F_m t_m^{-1/2} t^{1/2}, & t < t_m \\ F_m t_m t^{-1}, & t > t_m \end{cases} \quad (1)$$

This formula may not accurately represent the full complexity of the radio light curve evolution. However, it is good enough to determine the approximate values for the peak flux density F_m and the time of the peak t_m . These fitted values of peak flux density and peak times are provided in Table 3. All of the values quoted are in the observer’s frame. In our sample there are 24 radio afterglows for which we detect a small excess of radio emission at early times ($t < 3$ days) compared to the fit in Equation 1. We suspect that this excess may be the result of a separate reverse shock component. We will investigate this hypothesis in a separate paper. To avoid a possible reverse shock peak, we took the following precautions: If the light curve indicated two peaks, one before 3 days and one after that, we fit the later peak; If the best fit peak flux density was within first 3 days, we exclude it as this could be the possible reverse shock emission. The early-peaked light curve of GRB 060218 is included as the lone exception since it has a very low redshift, and hence the peak before day 3 could still come from the forward shock. For the afterglows which had less than 3 detections, we chose the value of highest flux density. In the case of single detection point at a particular frequency, we simply chose that value. There were 3 afterglows in 22.5 GHz band, 4 afterglows in 15 GHz band, 7 afterglows each in 8.5 and 4.9 GHz bands and 1 afterglow in 1.4 GHz band with single detection points. The second set of entries in Table 3 (i.e. after the horizontal line) represent the flux density values taken directly from the data, and hence do not have the best-fit errors. Rest frame peak times were obtained for the bursts with known redshift by using $t_m/(1+z)$. We do not estimate the rest frame peak time for bursts with unknown redshifts.

Table 3

The radio peak flux densities and the time of peak for radio afterglows

GRB	Freq. GHz	Peak Flux (F_m) μJy	Peak time (t_m) days	$t_m/(1+z)$ days
970508	1.43	381 ± 19	179.1 ± 7.6	97.6 ± 4.1
970508	4.86	780 ± 13	57.6 ± 0.9	31.4 ± 0.5
970508	8.46	958 ± 11	37.2 ± 0.4	20.3 ± 0.2
970828	8.46	144 ± 31	7.8 ± 1.8	4.0 ± 0.9
980329	4.86	171 ± 14	91.5 ± 11.3	22.9 ± 2.8
980329	8.46	332 ± 11	33.5 ± 1.4	8.4 ± 0.4
980425	1.38	22260 ± 195	47.1 ± 0.5	46.7 ± 0.5
980425	2.5	31621 ± 265	32.7 ± 0.3	32.4 ± 0.3
980425	4.8	38362 ± 337	18.3 ± 0.1	18.1 ± 0.1
980425	8.64	39360 ± 557	12.7 ± 0.1	12.6 ± 0.1
980519	4.86	330 ± 47	17.9 ± 2.4	...
980519	8.46	205 ± 23	12.6 ± 1.3	...
980703	1.43	263 ± 81	25.4 ± 5.5	12.9 ± 2.8
980703	4.86	1055 ± 30	9.1 ± 0.2	4.6 ± 0.1
980703	8.46	1370 ± 30	10 ± 0.2	5.1 ± 0.1
981226	8.46	137 ± 34	8.2 ± 1.6	3.9 ± 0.8
990510	8.46	255 ± 34	4.2 ± 0.5	1.6 ± 0.2

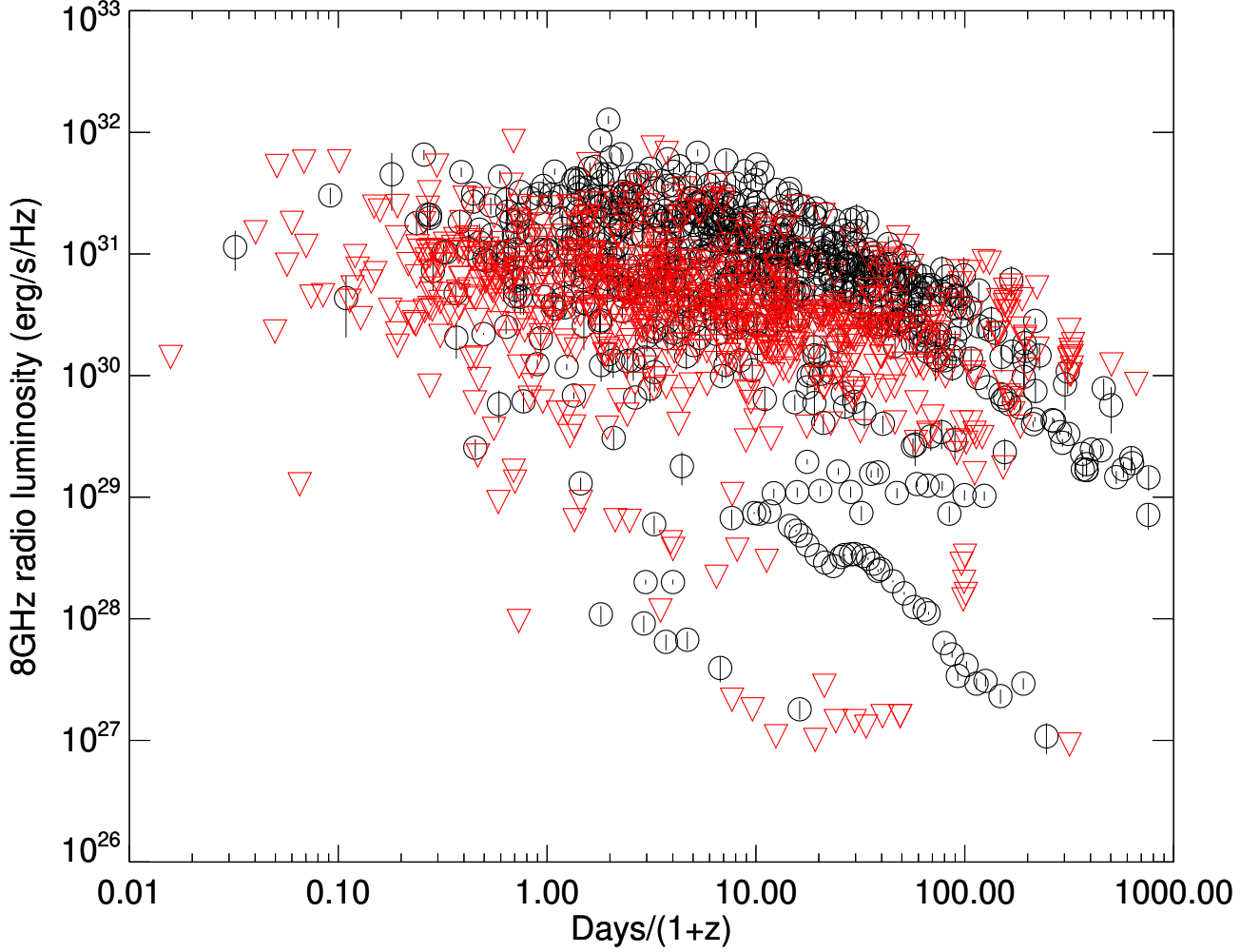


Figure 6. The k -corrected radio spectral luminosities at 8.5 GHz for radio-detected afterglows (black circles) versus non-detected 3-sigma luminosity upper limits (red triangles) with respect to the rest frame time. The luminosity curve for the average cosmological burst varies over a small range, but there are also a number of low-luminosity events.

Table 3 — *Continued*

GRB	Freq. GHz	Peak Flux (F_m) μ Jy	Peak time (t_m) days	$t_m/(1+z)$ days
991208	1.43	263 ± 49	8.9 ± 1.8	5.2 ± 1.1
991208	4.86	845 ± 48	12.8 ± 0.6	7.5 ± 0.4
991208	8.46	1804 ± 24	7.8 ± 0.1	4.6 ± 0.1
000301C	8.46	520 ± 24	14.1 ± 0.5	4.6 ± 0.2
000418	4.86	897 ± 39	27 ± 1	12.7 ± 0.5
000418	8.46	1085 ± 22	18.1 ± 0.3	8.5 ± 0.1
000911	8.46	263 ± 33	3.1 ± 0.3	1.5 ± 0.1
000926	4.86	460 ± 31	16.9 ± 1.5	5.6 ± 0.5
000926	8.46	629 ± 24	12.1 ± 0.5	4.0 ± 0.2
001018	8.46	590 ± 68	4.7 ± 0.6	...
010222	8.46	93 ± 25	16.8 ± 3.5	6.8 ± 1.4
010921	4.86	161 ± 20	31.5 ± 3.3	21.7 ± 2.3
011030	4.86	121 ± 19	19.4 ± 2.5	...
011030	8.46	139 ± 9	23.7 ± 1.4	...
011121	8.7	655 ± 40	8.1 ± 0.7	5.9 ± 0.5
011211	8.46	162 ± 13	13.2 ± 1.6	4.2 ± 0.5
020405	8.46	113 ± 17	18.2 ± 3.7	10.8 ± 2.2
020819B	8.46	291 ± 21	12.2 ± 1.1	8.7 ± 0.8
020903	4.86	782 ± 28	36.7 ± 1.3	29.4 ± 1.0
021004	4.86	470 ± 26	32.2 ± 1.4	9.7 ± 0.4
021004	8.46	780 ± 23	18.7 ± 0.5	5.6 ± 0.2
021004	15	1308 ± 260	4.1 ± 0.8	1.2 ± 0.2
021004	22.5	1614 ± 52	8.7 ± 0.3	2.6 ± 0.1
021206	4.86	480 ± 69	7 ± 0.8	...
030226	8.46	171 ± 23	6.7 ± 1	2.2 ± 0.3

Table 3 — *Continued*

GRB	Freq. GHz	Peak Flux (F_m) μ Jy	Peak time (t_m) days	$t_m/(1+z)$ days
030329	1.43	2232 ± 30	78.6 ± 2.1	67.3 ± 1.8
030329	4.86	10337 ± 33	32.9 ± 0.1	28.2 ± 0.1
030329	8.46	19567 ± 28	17.3 ± 0.1	14.8 ± 0.1
030329	15	34042 ± 84	10.9 ± 0.1	9.3 ± 0.1
030329	22.5	49596 ± 66	8.4 ± 0.1	7.2 ± 0.1
030329	43	59318 ± 177	5.8 ± 0.1	5.0 ± 0.1
030723	8.46	204 ± 40	75 ± 10.6	...
031203	1.43	929 ± 60	65.5 ± 5.3	59.3 ± 4.8
031203	4.86	828 ± 28	58.4 ± 2.1	52.9 ± 1.9
031203	8.46	724 ± 19	48 ± 1.3	43.4 ± 1.2
041219A	4.86	473 ± 28	6.3 ± 0.9	...
050416A	4.86	485 ± 36	48.5 ± 3.5	29.4 ± 2.1
050416A	8.46	373 ± 36	49 ± 3.6	29.7 ± 2.2
050509C	8.46	344 ± 45	44.1 ± 5.7	...
050603	8.46	377 ± 53	14.1 ± 1.8	3.7 ± 0.5
050713B	4.86	424 ± 34	21 ± 2.2	...
050713B	8.46	343 ± 24	14.1 ± 0.9	...
050820A	8.46	150 ± 31	9.4 ± 1.9	2.6 ± 0.5
050904	8.46	76 ± 14	35.3 ± 1.5	4.8 ± 0.2
051022	8.46	268 ± 32	5.2 ± 0.7	2.9 ± 0.4
060218	4.86	245 ± 50	3.8 ± 0.7	3.7 ± 0.7
060218	8.46	471 ± 83	2 ± 0.3	1.9 ± 0.3
070125	8.46	1028 ± 16	84.1 ± 2	33.0 ± 0.8
070125	15	1250 ± 81	18.6 ± 1.4	7.3 ± 0.5
070125	22.5	1778 ± 75	13.6 ± 0.5	5.3 ± 0.2

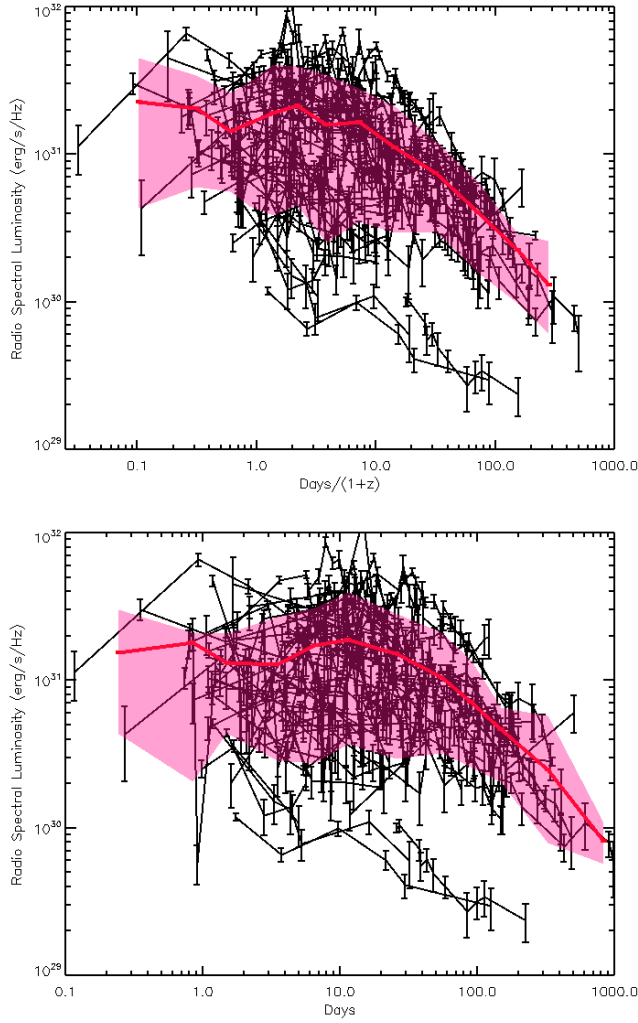


Figure 7. *Upper panel:* The radio light curves at 8.5 GHz for the long-duration, cosmological GRBs in the rest frame time. The red solid line represents the mean light curve. The pink shaded area represents the 75% confidence band. Lower panel shows the same plot for time in the observer's time frame.

Table 3 — *Continued*

GRB	Freq. GHz	Peak Flux (F_m) μJy	Peak time (t_m) days	$t_m/(1+z)$ days
070612A	4.86	580 ± 20	140.3 ± 5.8	86.8 ± 3.6
070612A	8.46	1028 ± 16	84.1 ± 2	52.0 ± 1.2
071003	8.46	616 ± 57	6.5 ± 0.5	2.5 ± 0.2
071010B	4.86	227 ± 114	12.5 ± 4.4	6.4 ± 2.3
071010B	8.46	341 ± 41	4.2 ± 0.5	2.2 ± 0.3
080603A	8.46	207 ± 26	5.2 ± 1.8	1.9 ± 0.7
081221	8.46	174 ± 27	8.9 ± 1.7	...
090313	8.46	435 ± 22	9.4 ± 0.5	2.1 ± 0.1
090323	8.46	243 ± 13	15.6 ± 1	3.4 ± 0.2
090328	8.46	686 ± 26	16.1 ± 0.7	9.3 ± 0.4
090423	8.46	50 ± 11	33.1 ± 6.3	3.6 ± 0.7
090424	8.46	236 ± 37	5.2 ± 0.7	3.4 ± 0.5
090715B	8.46	191 ± 36	9.2 ± 2.3	2.3 ± 0.6
090902B	8.46	84 ± 16	14.1 ± 2.6	4.9 ± 0.9
091020	8.46	399 ± 21	10.9 ± 0.6	4.0 ± 0.2
100414A	8.46	524 ± 19	8 ± 0.3	3.4 ± 0.1
100418A	4.86	522 ± 83	70.3 ± 8.1	43.4 ± 5.0
100418A	8.46	1218 ± 12	47.6 ± 0.6	29.4 ± 0.4
100814A	4.5	496 ± 24	13 ± 1	5.3 ± 0.4
100814A	7.9	613 ± 23	10.4 ± 0.4	4.3 ± 0.2
990510	4.86	177	9.2	3.5
991208	15	3100	5.4	3.2

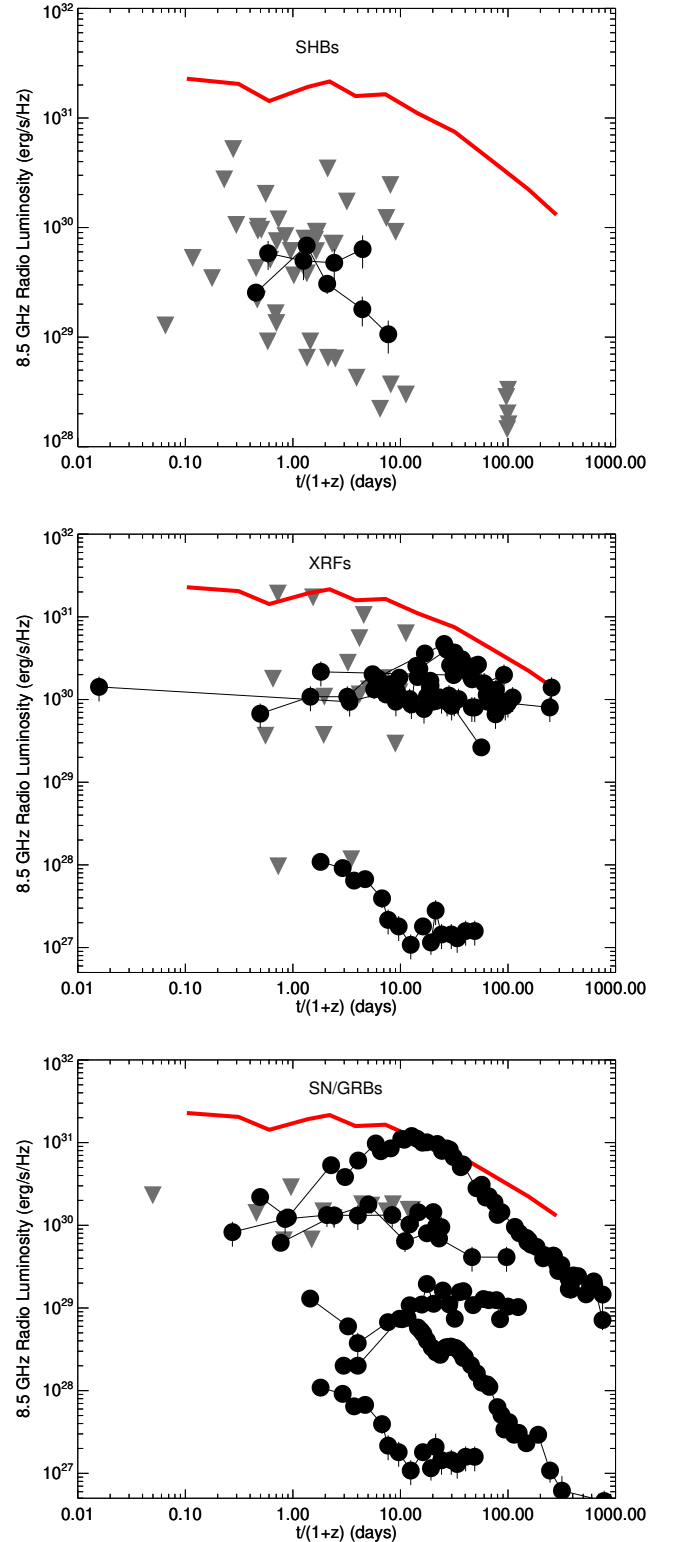


Figure 8. A compilation of radio luminosity curves in the rest frame for three different populations of GRBs: short, hard bursts (top), X-ray flashes (middle), and supernova-GRB associations (bottom). Here black filled circles represent the detections and the grey filled triangles represent the upper limits. The red solid line represents the mean light curve for the long-duration, cosmological sample from Figure 7.

Table 3 — *Continued*

GRB	Freq. GHz	Peak Flux (F_m) μ Jy	Peak time (t_m) days	$t_m/(1+z)$ days
991216	4.86	126	17.4	8.6
991216	15	1100	1.3	0.6
000131	8.7	207	10.8	2.0
000210	8.46	93	8.6	4.6
000301C	4.86	240	4.3	1.4
000301C	15	660	3.6	1.2
000301C	22.5	884	4.3	1.4
000418	15	1350	12.3	5.8
000418	22.5	1100	14.6	6.9
000911	4.86	71	11.1	5.4
000926	15	820	4.7	1.5
000926	22.5	1415	7.2	2.4
001007	8.46	222	7.1	...
010222	4.86	144	2.3	0.9
010921	22.5	330	25.9	17.9
010921	8.46	229	27	18.6
011121	4.8	510	6.9	5.1
020305	8.46	76	22.9	...
020903	1.43	294	91	72.8
020903	8.46	1058	23.8	19.0
021206	8.46	137	68.6	...
030115A	4.9	89	6	1.7
030115A	8.46	83	7.3	2.1
030226	22.5	328	74	24.8
030227	8.46	64	6.6	...
030323	22.5	530	3.5	0.8
030418	8.46	69	27.7	...
030723	4.86	217	77.9	...
031203	22.5	483	13.5	12.2
050401	8.46	122	5.7	1.5
050525A	8.46	164	13.5	8.4
050603	4.86	196	6.5	1.7
050730	8.46	212	9.1	1.8
050824	8.46	152	7.4	4.0
051022	4.86	209	57	31.5
060116	8.46	363	28	...
060218	1.43	198	4.9	4.7
060218	22.5	250	3	2.9
060418	8.46	216	4.3	1.7
070125	4.86	308	27.9	11.0
071003	4.86	224	3.8	1.5
071020	8.46	141	3.2	1.0
081203B	8.46	162	7	...
081221	4.86	142	14.4	...
090313	4.86	361	7.9	1.8
100413A	8.46	80	8.8	...
100414A	4.86	420	38	16.0
100901A	4.5	331	4.9	2.0
100901A	7.9	440	4.9	2.0
100901A	33.6	378	11.9	4.4
100906A	8.46	215	5	1.8

In Figure 9, we plot the histogram for rest frame peak times at 8.5 GHz band. It is clear that most of the radio afterglows peak between 3–9 days in the rest frame. This could be due to the ν_m passing the radio frequencies around this time. Another possibility is that jet breaks in GRBs occur mostly around this time (see table 6 and references therein) and radio stops rising after the occurrence of jet break. In the Figure 9, we also plot the peak luminosity distribution of all the detected afterglows at all epochs in 8.5 GHz band. The luminosity distribution peaks in the range $10^{31} - 10^{32}$ erg s $^{-1}$ Hz $^{-1}$.

3.6. 1.4 GHz analysis

While there is much less data at 1.4 GHz than at 8.5 GHz, obtaining the afterglow properties at this frequency is still useful. There are a number of wide-field imag-

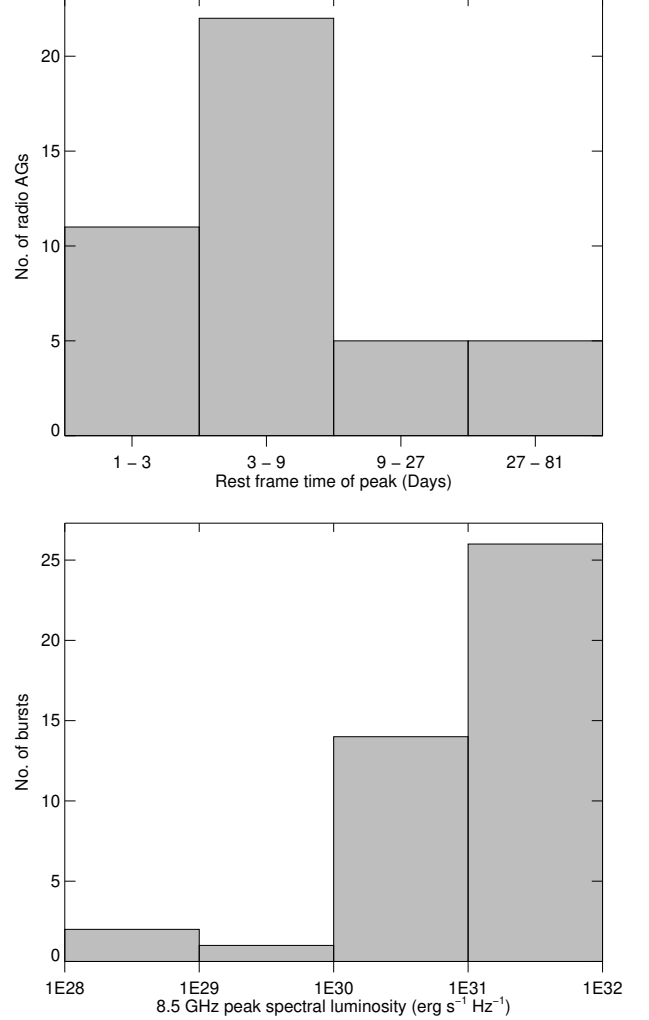


Figure 9. **Upper panel:** Histogram for the time-to-peak distribution in the rest frame for radio afterglows at 8.5 GHz. Most of the afterglows peak between 3–6 days. **Lower panel:** Distribution of peak radio luminosity at 8.5 GHz. Most of the bursts peak in the range $10^{31} - 10^{32}$ erg s $^{-1}$ Hz $^{-1}$.

ing instruments coming on line later this decade which are optimized to work at this frequency. This includes telescopes such as Australian Square Kilometre Array Pathfinder (ASKAP), the phased array feed Apertif on the Westerbork Synthesis Radio Telescope (WSRT), and the South African MeerKAT array.

A total of 310 measurements were made at this frequency for 55 GRBs. Out of 310 measurements, 125 resulted in detections corresponding to 12 GRBs. Thus in terms of number of GRBs detected, the detection rate is 22%, while the detection rate in terms of measurements made is 40%. However, this detection rate is likely an overestimate since our 1.4 GHz sample is strongly biased. Observations at this frequency were not taken unless a bright radio afterglow had been detected at 8.5 GHz.

In Figure 10, we plot our non-detections as 3- σ upper limits with respect to the epoch since explosion. We also overlay 1.4 GHz light curves of GRB 980703 (red curve) and GRB 970508 (blue curve). The plot shows that almost all the GRB upper limits are tightly clustered within one to two orders of magnitude (between 60

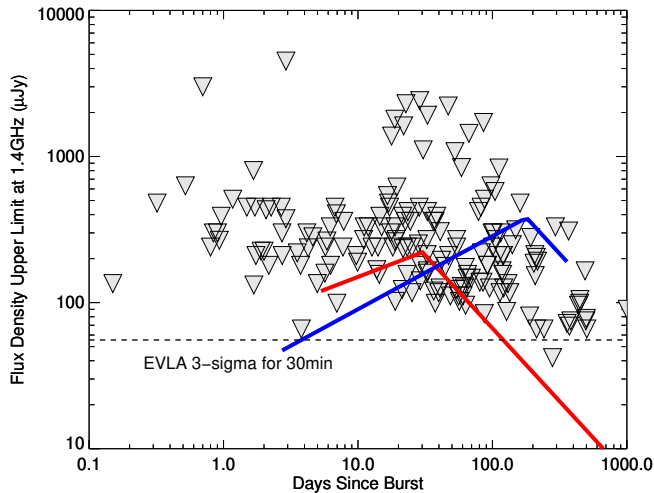


Figure 10. $3\text{-}\sigma$ upper limits at 1.4 GHz frequency band for all GRBs for which no afterglow was detected. The red line represent the light curve of event GRB 980703 and the blue line represents the light curve of event GRB 970508. We also plot the 1.4 GHz EVLA $3\text{-}\sigma$ upper limit for a 30 minute integration time.

μJy to around $3000 \mu\text{Jy}$). As illustrated in Figure 10, most of the observations would not have been capable of detecting afterglows from these representative GRBs. This figure suggests that radio searches are severely sensitivity limited at 1.4 GHz. With better sensitivity or more telescope time (see Figure 10), some improvement is expected detectable but as we show in §6, the optimal search strategy is to use higher observing frequencies.

In Figure 11, we plot the k -corrected 1.4 GHz radio spectral luminosities for the LGRBs and compare them with the $3\text{-}\sigma$ upper limits for the non-detections. The figure again clearly shows that no difference in the spectral luminosities between the detections and the upper limits, reinforcing the severe sensitivity limitation in resulting in various non-detections. The mean 1.4 GHz luminosity for the detected bursts is $2 \times 10^{30} \text{ erg s}^{-1} \text{ Hz}^{-1}$, and the mean $3\text{-}\sigma$ upper limit for the non-detections is $10^{31} \text{ erg s}^{-1} \text{ Hz}^{-1}$. Due to our strong selection bias these numbers likely overestimate the luminosity of a typical GRB afterglow at this frequency.

4. PARAMETER DISTRIBUTIONS

4.1. Redshift distribution

In our radio-selected sample of 304 GRBs we have 147 GRBs with known redshifts. This includes two bursts for which only a redshift range is known (GRB 980326 with $z = 0.9 - 1.1$ and GRB 980329 with $z = 2 - 3.9$). We have 99 GRBs with redshifts available in the post-*Swift* epoch as compared to just 48 bursts with known redshifts in pre-*Swift* epoch. The remaining 157 bursts had no redshift estimates, although 9 of them do have upper limits. In our sample, 59 bursts had $z \leq 1$ and 88 bursts had $z > 1$. GRB 090423 is the object with highest confirmed spectroscopic redshift of $z = 8.26$ (Tanvir et al. 2009; Salvaterra et al. 2009), whereas the highest photometric redshift in our sample ($z = 9.4$) is for GRB 090429B (Cucchiara et al. 2011). The highest redshift in pre-*Swift* sample is 4.5 for GRB 000131 (Andersen et al. 2000). GRB 980425 is the object with the lowest redshift with $z = 0.0085$ (Tinney et al. 1998). In Figure 12, we plot

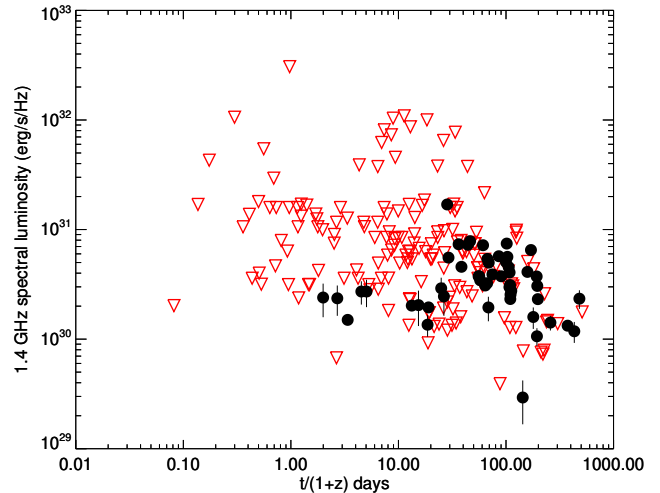


Figure 11. The detected k -corrected radio spectral luminosities at 1.4 GHz band (black circles) versus non-detected $3\text{-}\sigma$ luminosity upper limits (red triangles) with respect to the rest frame time since burst. The luminosity curve for the average cosmological burst is tightly clustered between $10^{30} - 10^{31} \text{ erg s}^{-1} \text{ Hz}^{-1}$.

the redshift distribution of our sample. We plot the pre-*Swift* and the post-*Swift* bursts for comparison. The figures indicate that the post-*Swift* bursts are mostly found in the redshift range of $0.8 - 6.4$ (71 bursts out of 99), whereas the maximum number of pre-*Swift* bursts lies in the redshift range of $0.4 - 3.2$ (39 bursts out of 44). Here we also plot the redshift distribution of radio-detected and non-detected sample. Most of the non-detected radio afterglows lie in range $z = 0.8 - 1.6$ and the detected radio afterglows lie between redshift of $0.8 - 3.2$. There is obviously no correlation between the redshift of the burst and its detectability in the radio band. Further support to the fact that the redshifts of the sample of radio detected GRBs and non-detected GRBs are not from different populations come from the Kolmogorov-Smirnov (K-S) test (Press et al. 1992). Comparing the redshifts of the two sample gives $P = 0.61$, strengthening the fact that the two samples are not from the different populations.

The average redshift of our sample is $\langle z \rangle_{total} = 1.8$. The average redshifts in pre- and post-*Swift* bursts are $\langle z \rangle_{pre} = 1.3$ and $\langle z \rangle_{post} = 2.0$, respectively. The mean redshift for the pre-*Swift* bursts is similar to the value $\langle z \rangle = 1.4$ derived by Jakobsson et al. (2006), however, they measure $\langle z \rangle = 2.8$ for a post-*Swift* optically-selected sample. Instrumental sensitivity may explain the origin of this bias in our radio-selected sample to slightly lower redshifts for post-*Swift*. However, Fynbo et al. (2009) has measured the average redshift of *Swift* sample to be $\langle z \rangle = 2.2$, based on a sample of 146 *Swift* bursts, which is closer to mean redshift of our radio selected sample. As first noted by Ciardi & Loeb (2000) and shown by Frail et al. (2006), the detection rate of radio afterglows is largely insensitive to redshift. This is shown in Figure 13, where we plot peak radio flux densities at 8.5 GHz band as a function of $(1+z)$. The red line shows the effect of the negative k -correction factor or radio afterglows, caused by the effects of spectral and temporal redshift, offsetting the diminution in distance. However, despite this effect we note that the mean peak flux den-

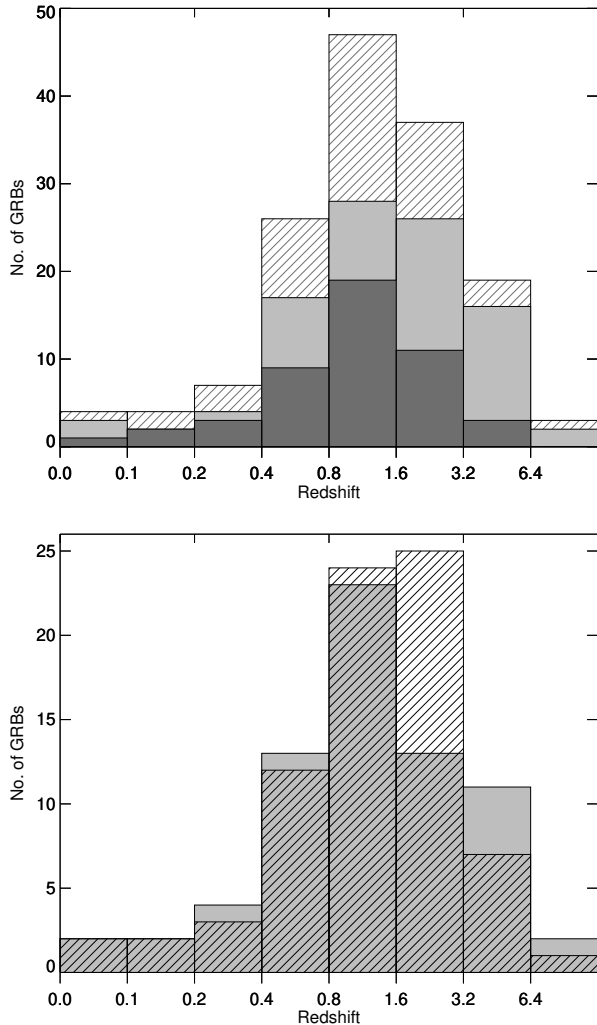


Figure 12. **Upper panel:** Redshift distributions for the post-*Swift* (light gray histogram) and the pre-*Swift* bursts (dark gray histogram). The average redshift of our sample is $z_{av} = 1.8$. The average redshifts in the pre- and post-*Swift* bursts are $\langle z \rangle_{pre} = 1.3$ and $\langle z \rangle_{post} = 2.0$, respectively. The redshift distribution of the complete sample is shown with the hatched histogram. **Lower panel:** The redshift distribution of the detected (hatched histogram) versus non-detected (filled histogram) radio afterglows for the complete sample.

sity at $z \sim 2.8$ is close to the sensitivity limit of existing instruments. Figure 13, however, shows that more sensitive telescopes, such as EVLA, will be able to detect higher- z bursts and enable us to test this hypothesis. In the mean time when discussing any distance-dependent effects for our sample we will adopt our derived redshifts rather than those in the literature.

4.2. Fluence distribution

Since the fluence of *Swift* bursts is available in the 15–150 keV energy range, all the fluences quoted in Table 6 are given in this range. We have converted fluences from the non-*Swift* telescopes to this energy range (15–150 keV) adopting the method explained in Nysewander et al. (2009). The fluences quoted in Table 6 are the fluences in the observer’s frame. In Figure 14, we plot the fluence distribution of the entire sample as well as for the radio-detected and non-detected sample. Even

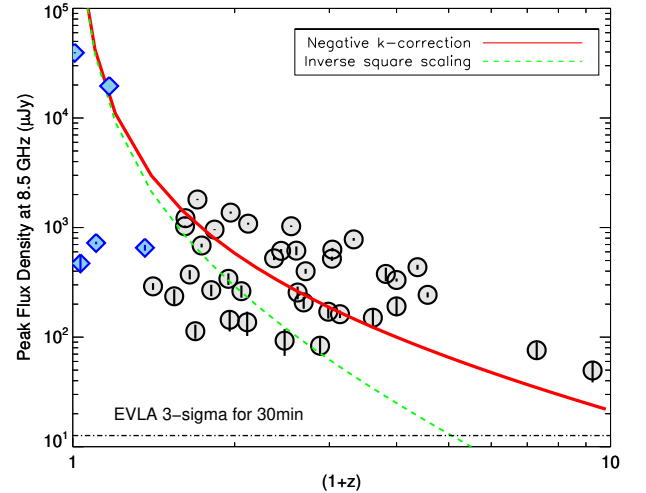


Figure 13. Radio peak flux density versus $(1+z)$ plot for radio afterglows with known redshifts. The radio measurements are in the 8.5 GHz band (in observer’s frame). Blue diamonds denote SNe/GRBs, while all the gray circles denote long-duration, cosmological GRBs. Red and green lines are the symbolic lines (with random normalization) indicating the two different scenarios of the flux density scaling. The green dashed line indicates if the flux density scales as simply the inverse square of the luminosity distance. The red thick line is the flux density scaling in the canonical afterglow model which includes a negative- k correction effect, offsetting the diminution in distance. $3\text{-}\sigma$ EVLA sensitivity is also plotted to show the EVLA capability to go deeper in z .

though both the samples peak in the range of $10^{-6} - 10^{-5}$ erg cm^{-2} , 176 out of 206 ($\sim 85\%$) non-detected radio afterglows have the fluence values $\leq 10^{-6}$ erg cm^{-2} , while 86% of the radio detected, i.e. 82 out of 95 bursts, have fluence values $\geq 10^{-6}$ erg cm^{-2} . Thus there is a clear overall trend of non-detected radio afterglows favoring the lower values of fluence as compared to the higher fluence values favored by the detected. The K-S test also gives the P value of $P = 2.61 \times 10^{-7}$ supporting the fact that the radio-detected and non-radio-detected GRB fluences are being derived from the different populations.

4.3. Energy distribution of the prompt GRB emission

We calculated the isotropic-equivalent γ -ray energies E_{iso}^{bol} for all bursts with known redshifts. The isotropic energies given in Table 6 are k -corrected bolometric energies. We adopt the rest-frame bandpass in the energy range 1 keV–10 MeV. We quote all the original references from which the energy values are taken. However, for those bursts in which this energy was not known, we obtained the information about the best-fit model of the prompt GRB spectrum from the GCN circulars archive⁴. The prompt emission is best fit by either band function (Band et al. 1993) or a cut-off power law function (CPL) or a simple power law (see Racusin et al. (2009) for details). We used these best fit parameters and adopted the method of Bloom et al. (2001) to estimate the k -corrected energy in 1 keV–10 MeV range. Since GRBs are collimated events, the beaming-corrected energy is smaller than the isotropic-equivalent energy. To obtain this, we identified all the GRBs with known jet breaks (t_j) from the literature. We also obtained all available

⁴ http://gcn.gsfc.nasa.gov/gcn3_archive.html

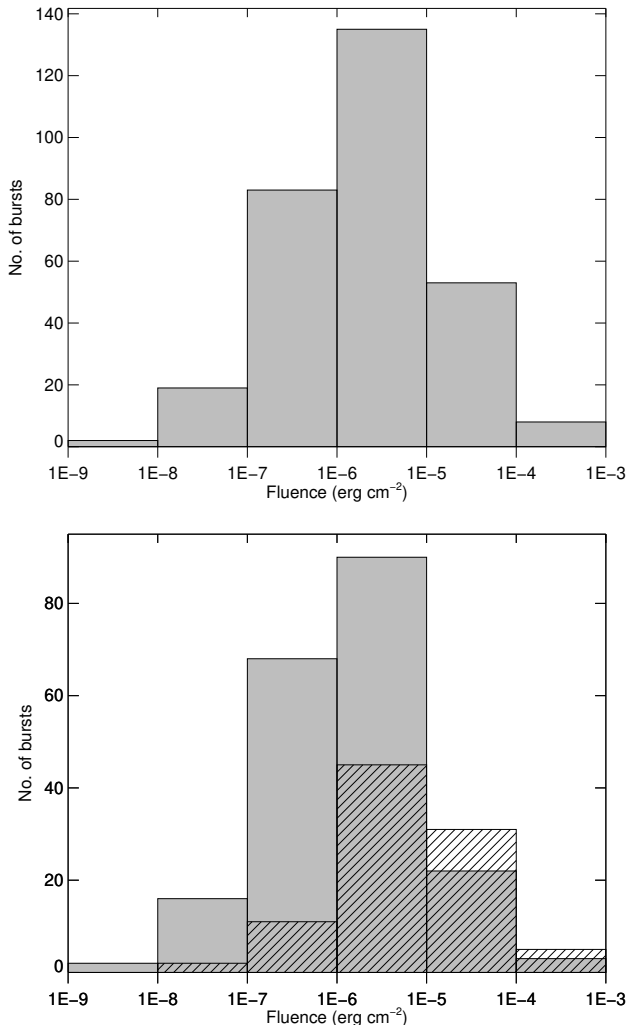


Figure 14. *Upper Panel:* Histogram of the fluence distribution for our entire sample. *Lower panel:* Fluence distribution of the radio-detected sample (hatched histogram) versus the non-detected sample (filled histogram).

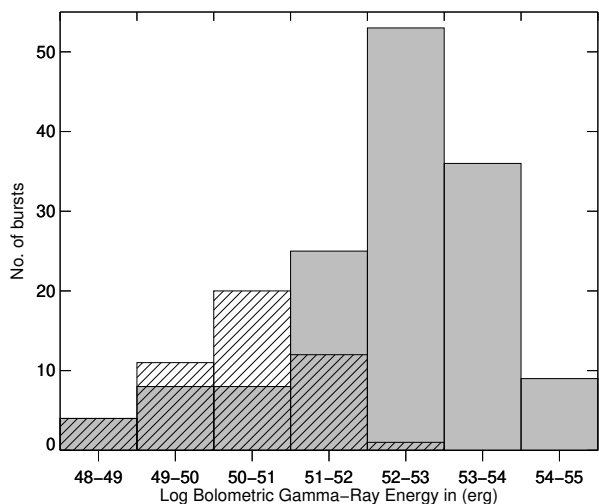


Figure 15. The isotropic energy distribution of our complete sample. Overlapped hatched histogram shows the beaming-corrected energy distribution.

circumburst densities n from the literature. If a GRB had a known jet break but no available density measurement, we assumed density $n = 1 \text{ cm}^{-3}$ (we denote it as [1] in Table 6). Once having values of t_j and n , we estimated the collimation angle θ_j using (Frail et al. 2001). The beaming fraction $f_b = (1 - \cos\theta_j) \approx \theta_j^2/2$ was estimated to calculate the beaming-corrected bolometric energies E_{true}^{bol} , where $E_{true}^{bol} = f_b E_{iso}^{bol}$.

In Figure 15, we plot the isotropic energy E_{iso}^{bol} distribution available for 144 GRBs of our sample (46 GRBs in pre-*Swift* epoch and 98 GRBs in post-*Swift* epoch). While maximum GRBs lie in the energy range of $10^{52} - 10^{53}$ erg, the energy range spread of the sample is between $1.6 \times 10^{48} - 4.1 \times 10^{54}$ erg, i.e. 7 orders of magnitude (this includes all the GRBs including SHBs, XRFs and SN-GRBs). This energy distribution and wide spread to lower energies is characteristic of other large samples (Kann et al. 2010). The figure also shows the beaming corrected energy distribution (hatched histogram). There are only 48 GRBs in our sample (excluding upper limits) which had beaming-corrected energies estimated. Even though most of the GRBs lie between energy range $10^{50} - 10^{51}$ erg, the total spread in energy range is from $2.4 \times 10^{48} - 1.4 \times 10^{52}$ erg. This distribution is similar to the previous studies (e.g. Racusin et al. 2009).

In Figure 16, we plot the isotropic-equivalent and beaming corrected γ -ray energies for the radio-detected and non-detected sample. In case of isotropic energies, the non-detected sample peaks at $10^{52} - 10^{53}$ erg, whereas, the detected sample peaks at $10^{53} - 10^{54}$ erg range. While 60 out of 95 radio detected bursts have isotropic-equivalent $\geq 10^{53}$ erg, only 9 out of 206 radio non-detected bursts have energies above 10^{53} erg. For beaming corrected energies, the non-detected sample peaks at $10^{49} - 10^{50}$ erg, whereas, the detected sample peaks at $10^{50} - 10^{51}$ erg range. This indicates that bolometric energies can indeed be a good indicator of the radio detectability of a burst. The K-S test gives the P values for the isotropic and beaming corrected energies of the two samples to be $P = 9.97 \times 10^{-7}$ and $P = 3.47 \times 10^{-3}$, respectively (see Table 4). This implies that the two samples are inconsistent with being drawn from the same distribution and γ -ray energetics is indeed a good indicator of the radio detectability of a burst, with isotropic-equivalent energy being the stronger indicator.

4.4. Distribution of X-ray and optical fluxes

The X-ray fluxes (F_X^{11h}) quoted in Table 6 are in the energy range 0.3–10 keV. The X-ray fluxes of *BepoSAX* bursts are given in the energy range of 1.6–10 keV range. All X-ray fluxes are corrected for Galactic extinction and we quote the X-ray fluxes at a time of 11 hr after the burst. This is partly because most GRBs have measurements at this time but also because it is expected that the cooling frequency at this time will usually lie between the optical and X-ray frequencies (Nysewander et al. 2009). The afterglow flux will then be independent of the circumburst density for observing frequencies above the cooling frequency. We obtained most of our X-ray fluxes at 11 hr from Gehrels et al. (2008); de Pasquale et al. (2006); Sakamoto et al. (2008,

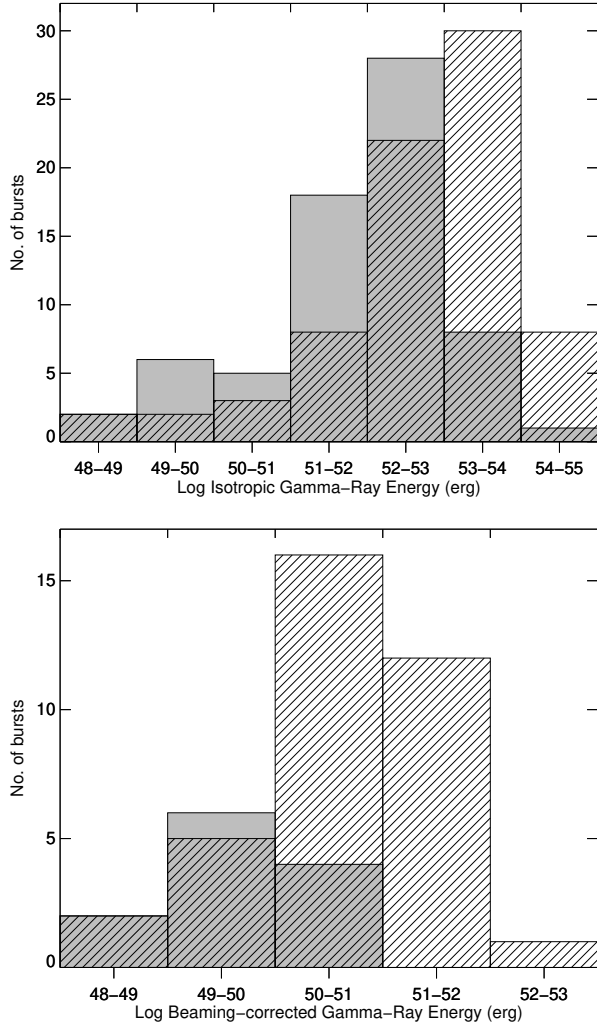


Figure 16. Upper panel shows the isotropic-equivalent γ -ray energy distribution of the radio-detected sample (hatched histogram) versus the non-detected sample (gray filled histogram). Lower panel shows the same distribution for the beaming corrected energies.

2011). However, for the bursts in which the flux at 11 hr was not available, we obtained the X-ray light curve from the *Swift* XRT Lightcurve Repository (Evans et al. 2007) and derived the flux as close to 11 hr as possible (i.e. within ± 0.5 hr). If the flux at ~ 11 hr was not available, we fit the X-ray light curve with a simple powerlaw and extrapolated the flux to 11 hr. This was done for 33 afterglows. Only in 5 cases, when the X-ray light curve was not available, did we extrapolated the available X-ray flux to 11 hr using temporal index (α_X , in $F_X \propto t^{\alpha_X}$) $\alpha_X = -1.17$ for long bursts and $\alpha_X = -1.22$ for SHBs (Nysewander et al. 2009).

Optical R band flux densities (F_R^{11h}) are also obtained at 11 hr in units of μJy . For those bursts in which we could not find the desired values from the published references, we used the GCN circulars and then extrapolated to the reported values at 11 hr using the best fit time decay index available. If a decay index was not available, we used a temporal slope of $\alpha_R = -0.85$ (in $F_R \propto t^{\alpha_R}$) for long bursts and $\alpha_R = -0.68$ for SHBs. The bursts for which an R-band magnitude was not available, we used

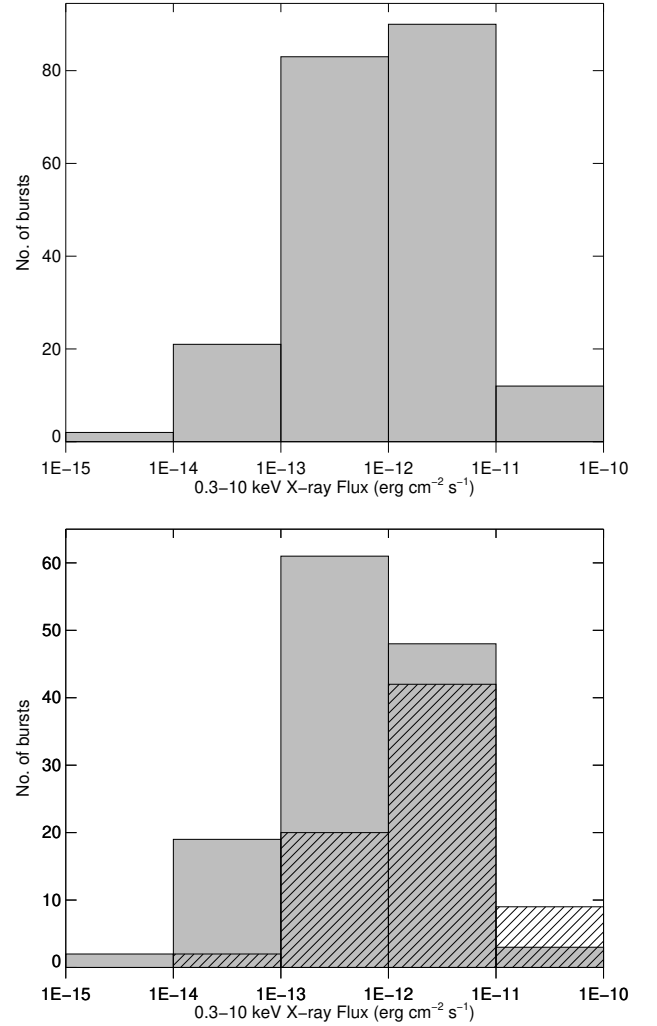


Figure 17. Upper panel: The distribution of the X-ray fluxes for our sample. Lower panel: This shows X-ray flux at 11 hr distribution of the radio-detected sample (hatched histogram) versus the non-detected sample (gray filled histogram).

Table 4

P values for Kolmogorov-Smirnov test for the radio detected versus non-detected GRB sample

Parameter	P value
Redshift	0.61
Isotropic equivalent γ -ray energy	9.97×10^{-7}
Beamed γ -ray energy	3.47×10^{-3}
Fluence	2.61×10^{-7}
X-ray flux (0.3–10 keV)	3.61×10^{-6}
Optical R -band flux density	1.30×10^{-9}

spectral index of $\beta_R = -1$ (in $f_R \propto \nu^{\beta_R}$) to convert the magnitudes into R band. We also corrected the flux densities for Galactic extinction using Schlegel et al. (1998). All the magnitudes were converted into μJy using online NICMOS unit conversion tool⁵.

In Figure 17, we plot the X-ray flux distribution of our sample which is spread between $10^{-15} - 10^{-10} \text{ erg cm}^{-2} \text{ s}^{-1}$. The majority of bursts have X-ray fluxes in the

⁵ http://www.stsci.edu/hst/nicmos/tools/conversion_form.html

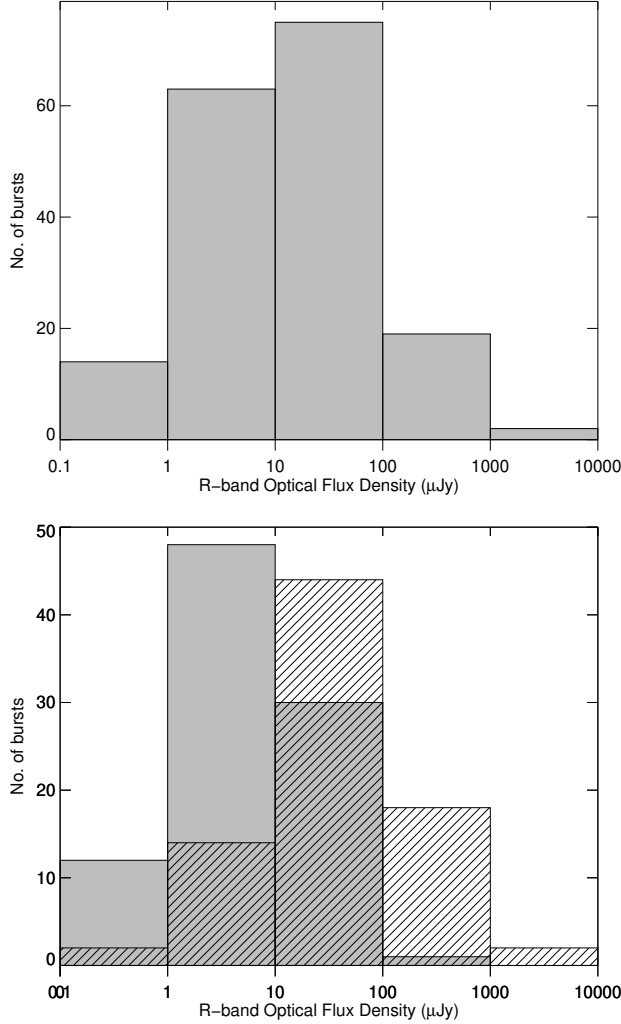


Figure 18. Upper panel shows the distribution of the optical flux densities for our sample. Lower panel shows the optical flux density distribution of the radio-detected sample (hatched histogram) versus the non-detected sample (gray filled histogram).

range $10^{-12} - 10^{-11}$ erg cm $^{-2}$ s $^{-1}$. Lower panel shows the X-ray flux at 11 hr of the radio-detected and non-detected samples. While the radio-detected sample peaks between $10^{-12} - 10^{-11}$ erg cm $^{-2}$ s $^{-1}$ range, the non-detected samples peaks at an order of magnitude less flux between the range $10^{-13} - 10^{-12}$ erg cm $^{-2}$ s $^{-1}$. In Figure 18, we plot the optical flux density distribution of our sample which ranges from 0.1 μ Jy to 10^4 μ Jy. Most of the optical bursts lie in 10–100 μ Jy range. In this figure, we also plot the optical R-band flux density at 11 hr for the radio-detected and non-detected sample. The non-detected sample peaks at 1–10 μ Jy, whereas, the detected sample peaks at 10–100 μ Jy.

On average, the X-ray fluxes of bursts are an indicator of radio detectability. Likewise, the dust-extinction corrected optical magnitude of the burst is also a potential indicator of the radio detectability of the burst. The K-S test also supports this fact with P values of $P = 3.61 \times 10^{-6}$ and $P = 1.30 \times 10^{-9}$ for the X-ray and the optical fluxes, respectively (Table 4).

5. CORRELATIVE PROPERTIES

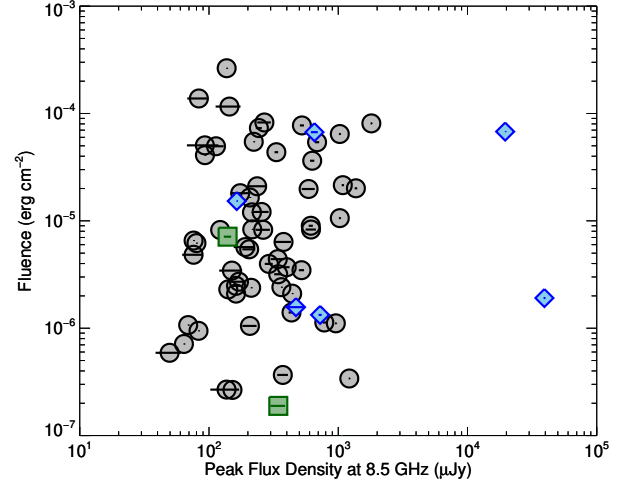


Figure 19. Peak radio flux densities at 8.5 GHz band taken from Table 3 on the X-axis and their corresponding fluences in 15–150 keV band are plotted on the Y-axis. Blue diamonds denote SN/GRBs and green squares denote XRFs, while all the gray circles denote long cosmological GRBs.

Here we proceed to look for correlations between the peak radio flux density (or luminosity) at 8.5 GHz band with various GRB properties (such as fluence, isotropic and beaming-corrected energy) and the X-ray and optical afterglow properties (redshift, flux density). We estimate the correlation in terms of the Pearson’s correlation coefficient, or R-index. The R-index varies between -1 to +1. A negative correlation coefficient indicates negative correlation between the quantities. An R-index close to 0 means no correlation or a weak correlation. R-index values of ≥ 0.5 indicates a significant correlation between the parameters. We use only LGRBs to obtain the correlation coefficient to maintain homogeneity for this correlation analysis.

In Figure 19, we plot the 15–150 keV fluences of radio detected GRBs against their corresponding peak radio flux densities at 8 GHz band from Table 3. There is no correlation between the two. The Pearson’s correlation coefficient, R-index, between the two is 0.02. The figure also shows that while the spread in fluence is four orders of magnitude, radio peak flux densities are tightly clustered.

We also plot the isotropic γ -ray energies E_{iso}^{bol} against their respective peak radio luminosities in Figure 20. There is no correlation between the radio spectral luminosity and the isotropic energy of GRBs with R-index of 0.12.

In Figure 21, we plot the X-ray fluxes at 11 hr for radio-detected GRBs against their corresponding peak radio flux densities at 8.5 GHz band from Table 3. There is no correlation between the two with a R-index value of -0.05. We also plot the R-band optical flux densities at 11 hr for the radio-detected GRBs against their corresponding peak radio flux densities at 8.5 GHz band from Table 3. The two parameters seem to be correlated. With a correlation index of 0.62, F_R^{11h} is the only parameter correlated with the peak strength of a radio afterglow. Despite this correlation, Figure 21 still illustrates the clustering of the radio points over a narrow flux density range.

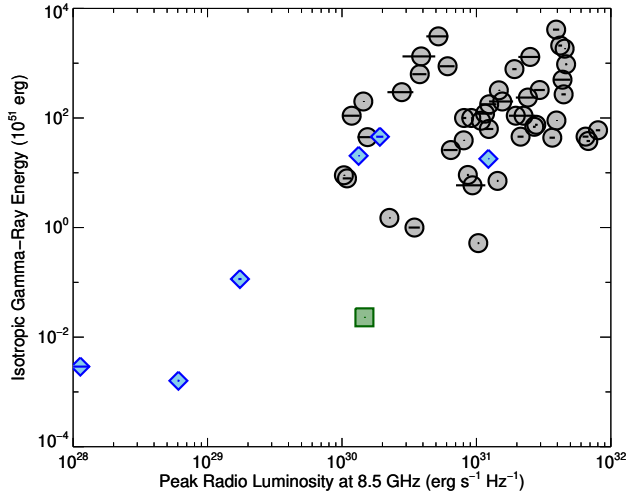


Figure 20. The peak radio luminosity at 8.5 GHz versus isotropic-equivalent γ -ray energies for various bursts. Here blue diamonds correspond to the SN/GRB events, green squares XRF events and gray circles are long cosmological GRBs.

Table 5
R-index correlation coefficient between various parameters of GRB afterglows

Parameter 1	Parameter 2	R-index
Peak radio flux density	Fluence	0.02
Peak radio luminosity	Isotropic bol. energy	0.12
Peak radio flux density	X-ray flux	-0.05
Peak radio flux density	Optical flux	0.62

In Table 5, we tabulate the R-index correlation between various GRB parameters. The correlation coefficients vary between -1 to +1. The correlation coefficient values clearly indicate that the strength of the peak radio flux density does not depend upon the fluence, isotropic γ -ray energy or the X-ray flux. Only the optical flux density at 11 hr has a positive correlation with the peak strength of the radio afterglows.

6. SYNTHETIC RADIO LIGHT CURVES

In order to compare the properties of our radio-sample with predictions from the basic afterglow theory, we plot synthetic light curves of GRB radio afterglows and determine their dependence on various afterglow parameters such as density, kinetic energy, redshift and microscopical shock parameters. In Figure 22, we plot the radio afterglow flux density at the median GRB redshift $z = 3$ (Jakobsson et al. 2006) and density $n = 10 \text{ cm}^{-3}$ for different frequencies i.e. 1.4 GHz, 8.5 GHz, 35 GHz (EVLA bands) and 250 GHz (ALMA band). Here we fix other parameters such as the isotropic kinetic energy $E_{KE,iso} = 10^{53} \text{ erg}$, the beaming angle $\theta_j = 0.2 \text{ rad}$, the electron energy density $\epsilon_e = 0.1$, the magnetic energy density $\epsilon_B = 1\%$, and the electron spectral index $p = 2.2$. The GRB parameters that we use here are good averages from the afterglow broadband modeling (Panaitescu & Kumar 2001; Yost et al. 2003).

While not unique, the 8.5 GHz light curve in Figure 22 reproduces the average properties of our radio-selected sample derived in §3. The mean flux density (Table 2), the time-to-peak (§3.5) and the overall timescale of the

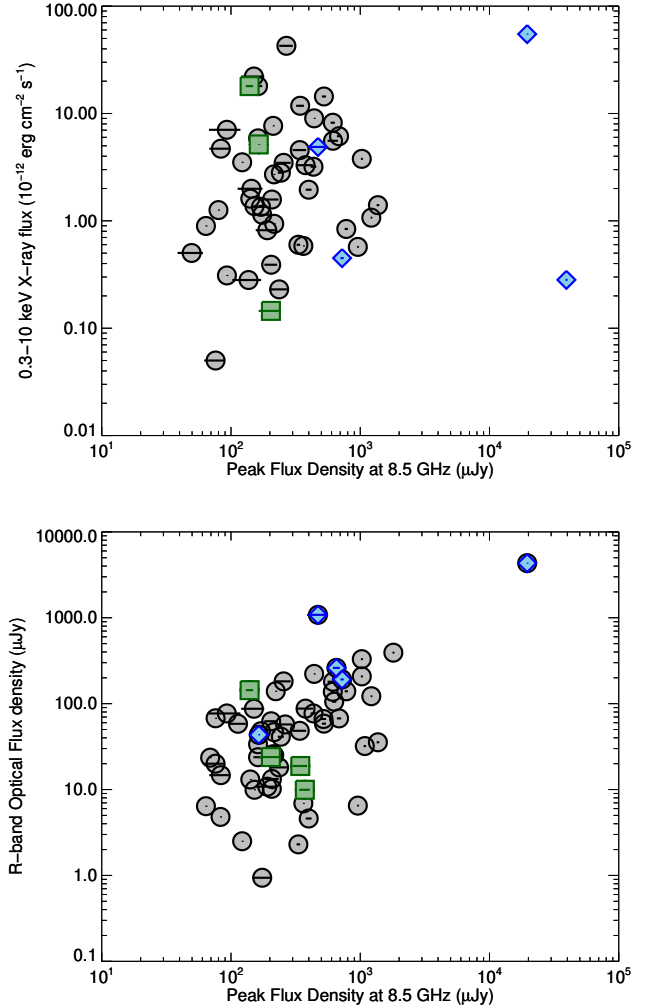


Figure 21. *Upper panel:* Peak radio flux densities at 8.5 GHz taken from Table 3 are on the X-axis and their corresponding X-ray fluxes at 11 hr in 0.3–10 keV band are plotted on the Y-axis. Blue diamonds denote SN/GRBs and green squares denote XRFs, while all the gray circles denote long cosmological GRBs. *Lower panel:* Peak radio flux density versus the R-band optical flux at 11 hrs.

decay is as seen in the data. The initial rise of the synthetic light curve at 8.5 GHz is steeper than the canonical long-duration event (Figure 7), but as we have already noted (e.g. §3.3), this may be the result of an additional early emission component, possibly a reverse shock. The light curves in this figure are generated with only a forward shock component.

With this close agreement between the model and the data, we can now investigate the effects of changing the observing frequency. As expected, there is a clear trend of increasing peak flux density and decreasing time-to-peak with increasing frequency. For illustration we compute the EVLA $3\text{-}\sigma$ sensitivities at 1.4 GHz, 8.5 GHz and 35 GHz bands and ALMA band-6 for a 1-hr integration. These are $40 \mu\text{Jy}$, $9 \mu\text{Jy}$ and $17 \mu\text{Jy}$, and $42 \mu\text{Jy}$, respectively. The challenges of detecting typical long-duration event events below 1.4 GHz are immediately apparent. For the above given set of parameters, which are used to generate these light curves, EVLA, ASKAP, and WSRT/Apertif will not be able to detect radio af-

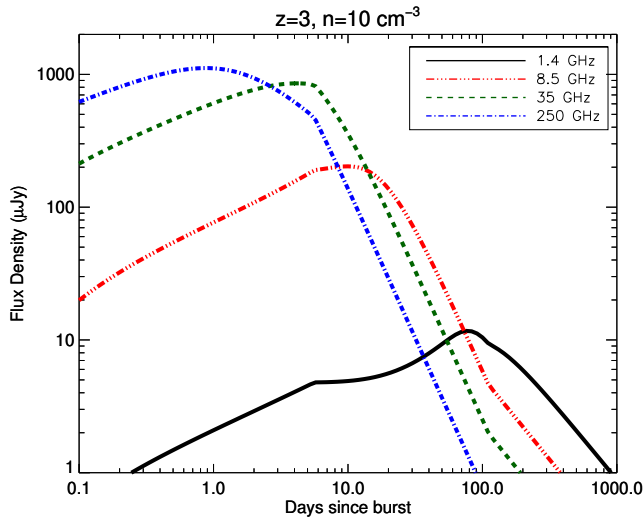


Figure 22. Plot of radio flux density light curves for a “standard” GRB afterglow at various frequencies for a redshift $z = 3$ and density of 10 cm^{-3} . See text for more details.

terglows at 1.4 GHz unless they are observed for long integration times. Higher frequencies are clearly favored for detecting radio afterglows. We expect a large increase in the fraction of detectable radio afterglows with ALMA and the EVLA, should higher observing frequencies be used than in the past.

In Figure 23, we derive the dependence of the radio afterglow light curve on various parameters, such as density, microscopic parameters and kinetic energy. Since there is only a weak dependence on the electron energy density (ϵ_e) and electron spectral index (p), we do not show these plots here.

We adopt the constant density model for the circumburst medium to generate these synthetic light curves. The plots are made for a frequency of 8.5 GHz to enable comparison with our existing sample. As noted above, future EVLA observations would better to be conducted at higher frequencies. Increasing the centimeter radio frequency modifies the flux density and timescales somewhat but it does not affect the dependencies that we see below.

In the top left panel of Figure 23 we plot the synthetic light curves of radio afterglows for various density values n at a redshift $z = 3$. We fix other parameters as $E_{KE,iso} = 10^{53}$ erg, $\theta_j = 0.2$ rad, $\epsilon_e = 0.1$, $\epsilon_B = 1\%$, and $p = 2.2$. The radio afterglow brightness is a strong function of density. The flux density depends upon two competing effects. There is an initial increase in radio emission due to the enhanced synchrotron emission as the density increases but as the density continues to increase there is a reduction in the radio flux density due to the increasing synchrotron self-absorption effect. The figure shows that the radio afterglow is brightest for densities between $n = 1 - 10 \text{ cm}^{-3}$; suggesting that existing radio samples are biased to a narrow range of circumburst densities. At lower densities, the afterglow is intrinsically weak, whereas at higher densities, synchrotron self-absorption effects are suppressing the radio afterglow strength for a long time. This may also explain why some of the bright GRBs are dim in radio band. They may need late-time observations in order to be detected.

To determine the dependence of radio afterglow as a

function of ϵ_B , we plot the lightcurves for various values of fractional magnetic energy density in the top right plot of Figure 23. We derive the light curves for a burst at a $z = 3$ and for circumburst density $n = 10 \text{ cm}^{-3}$. We fix rest of the parameters as $E_{KE,iso} = 10^{53}$ erg, $\theta_j = 0.2$ rad, $\epsilon_e = 0.1$, and $p = 2.2$ as before. There is a clear trend. The higher the magnetic energy density, the brighter the radio afterglow peak. This is not surprising since the synchrotron emission is more efficient in high magnetic field. This trend is seen from $n = 0.1 \text{ cm}^{-3}$ to $n = 10 \text{ cm}^{-3}$ but it does not continue to the higher density $n = 100 \text{ cm}^{-3}$. At higher densities the peak flux density does not increase dramatically with increasing ϵ_B , there is only a shift of the time-to-peak to later times. This is due to the effects of the large synchrotron absorption frequency which suppresses the emission.

As expected, the radio afterglow strength strongly depends upon the kinetic energy of the burst (lower left panel of Figure 23). The curve with an isotropic energy of 10^{53} erg is identical to that in Figure 22 and we noted above that it provided a reasonable description of the average properties of our sample. The beaming-corrected energy for this burst is 2×10^{51} erg, a value that is at least consistent with the kinetic energy derived from radio calorimetry (Berger et al. 2004b; van der Horst et al. 2008).

In the lower right panel of the Figure 23, we determine the redshift dependence of radio afterglows for values of $z = 0.5, 1, 3, 5$ and 8 . Here we fix other parameters as $E_{KE,iso} = 10^{53}$ erg, $\theta_j = 0.2$ rad, $\epsilon_e = 0.1$, $\epsilon_B = 1\%$, $n = 10 \text{ cm}^{-3}$, and $p = 2.2$. Between the redshifts of 0.5 to 3 , the lightcurves get progressively fainter with decreasing redshift, but beyond about $z \sim 3$, the negative- k correction effects come into effect and the peak radio flux density falls only slightly with increasing redshift (see also §4.1). Thus, essentially all the bursts with kinetic energies $E_{KE,iso} \geq 10^{53}$ erg should be easily detectable with less than 20-30 minutes exposure with the EVLA at any redshift. In Figure 25, we also plot some of the LGRBs with known redshifts between $z = 0.8$ to $z = 8.3$ and show the capability of the EVLA to observe these bursts for a much longer duration.

Finally in Figure 24 we show flux density relationships for our standard afterglow model at X-ray, optical and radio wavelengths. These curves are not meant to be a complete exploration of the phase space but they represent the broad behaviors to be expected with time. The correlations (or lack thereof) in §5 can now be understood. As we have already noted, our radio sample is sensitivity limited. Most 8.5 GHz measurements are tightly clustered between $30 \mu\text{Jy}$ to around $400 \mu\text{Jy}$ with a mean of about $170 \mu\text{Jy}$. In contrast, optical and X-ray measurements are sensitive to flux densities which vary over many more orders of magnitude. We can see from the figures that this limitation of the radio sample restricts the time range over which the correlations can be investigated. There is an additional complication in Figure 24 and that is the temporal evolution of the radio flux density is complex compared to the nearly monotonic behavior at X-ray and optical wavelengths.

7. ALMA PREDICTIONS

Our radio-selected catalog also contains millimeter and submillimeter radio observations. There are

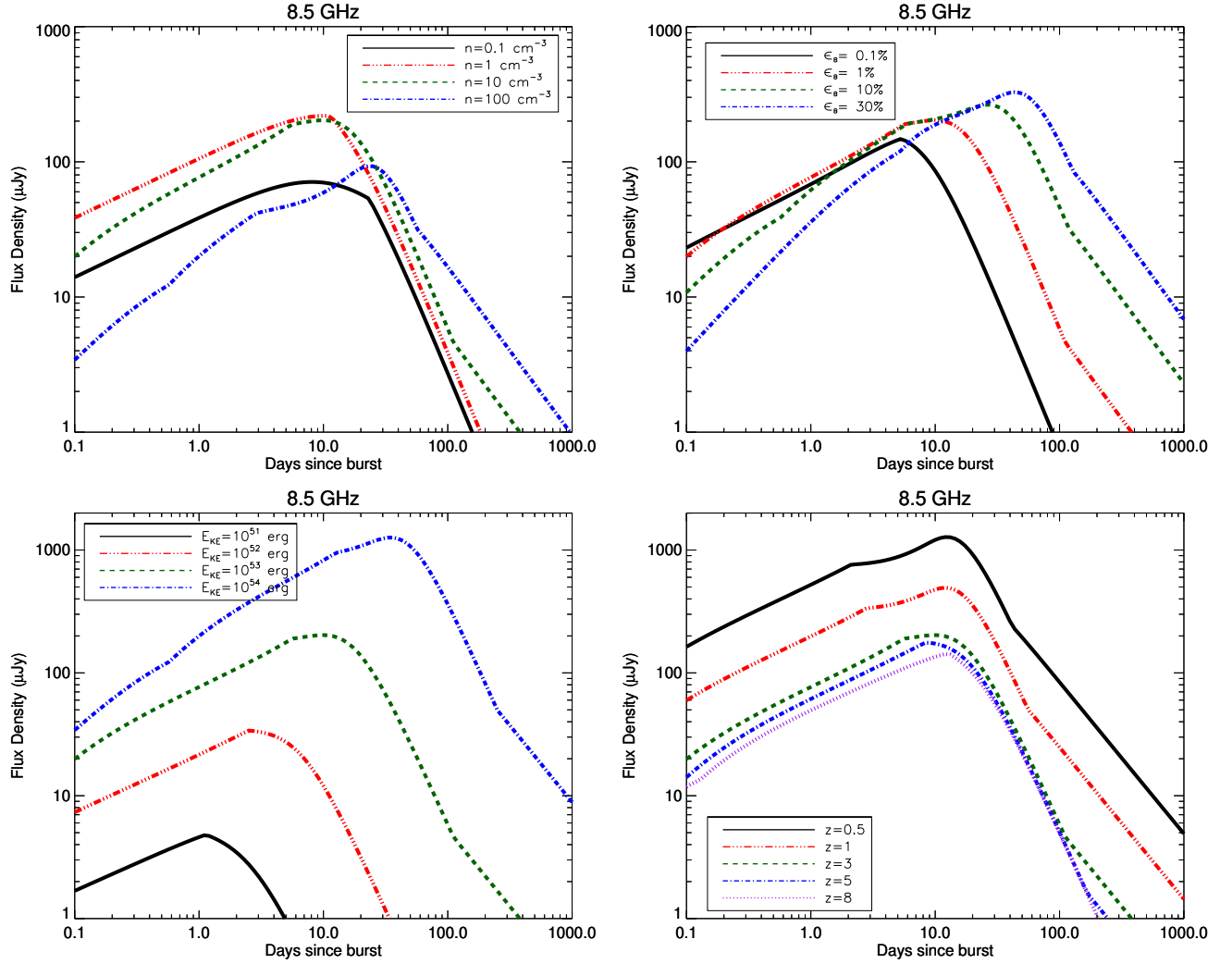


Figure 23. 8.5 GHz synthetic radio light curves for various values of density (top left), magnetic energy density (top right), isotropic kinetic energy (lower left) and redshift (lower right). EVLA sensitivity in this band for 1 hr integration time is $9 \mu\text{Jy}$.

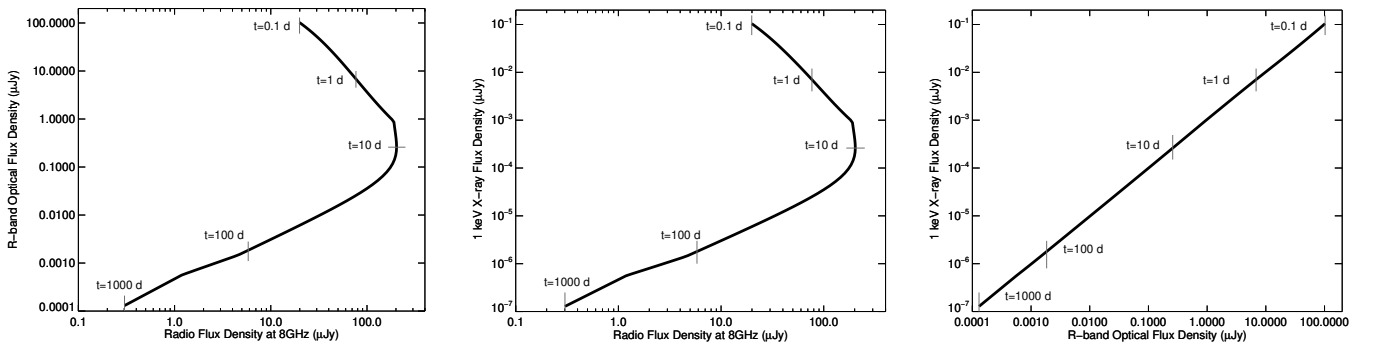


Figure 24. Synthetic model radio flux density values at 8.5 GHz with respect to the corresponding R-band optical (left panel) and 1 keV X-ray (middle panel) flux densities. Time stamps are indicated from 0.1 to 1000 days. For comparison, the right panel shows the plot of optical versus X-ray flux densities. The model is the same as that used in Fig. 22. See text for more details.

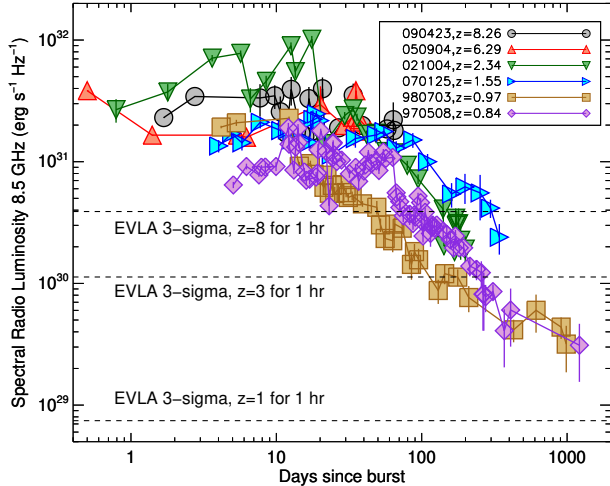


Figure 25. 8.5 GHz radio light curve luminosity plots for some radio afterglows at different redshifts. We also plot the 1 hr EVLA 3- σ sensitivity limit at a $z = 1, 3$ and 8 .

186 mm/submm observations of 30 GRBs in our database so an analysis similar to the one we have done for the centimeter data is possible. However, de Ugarte Postigo et al. (2011b) have recently done a comprehensive analysis of all mm and submm data available for GRB afterglows. It is more useful to simply summarize their findings and then compare their results with a typical GRB afterglow model (Figure 22) and explore the dependence of the radio millimeter afterglow brightness as a function of density, redshift, energy and ϵ_B (e.g. §6).

The first mm/submm observations of GRBs were undertaken shortly after the discovery of the cm afterglow (Smith et al. 1997a; Shepherd et al. 1998; Bremer et al. 1998). In subsequent compilations (Smith et al. 1999, 2005) it was well-established that the mm/submm detection rate was strongly limited by sensitivity, with most detected events with flux densities in excess of one or two milliJanskys. The situation has not improved significantly in subsequent years but the upcoming ALMA represents a jump of two orders of magnitude in continuum sensitivity.

de Ugarte Postigo et al. (2011b) report a detection rate of 25% for a sample of 102 mm/submm afterglows. de Ugarte Postigo et al. (2011b) use the detections and upper limits (assuming a Gaussian distribution) to make a rough estimate of the mean peak mm/submm flux density of 0.3 mJy. The average redshift of their sample is $z_{av} = 1.99$ and the average peak luminosity is $10^{32.1 \pm 0.7}$ erg s^{-1} Hz $^{-1}$.

Using typical GRB parameters, we showed in Figure 22) that a radio afterglow will be an order of magnitude brighter in the mm/submm (e.g. 250 GHz band) than in cm (e.g. 8.5 GHz). Support for this claim comes from average peak spectral luminosities which also differ by an order of magnitude (§3.5).

We also can explore synthetic light curves identical to the cm curves from §6 but applied to the ALMA band 6 (211–275 GHz band) as a function of various parameters. In the upper left panel of Figure 26, we plot the synthetic radio light curves of GRB afterglows for various values of density n at a redshift $z = 3$. We fix other parameters as

given in §6. The mm/submm radio afterglow is a strong function of density. Since the effects of synchrotron self-absorption are weak in mm/submm bands, there is no competing effect to reduce the emission at higher densities (unlike at cm bands). With its full collecting area, ALMA’s 3- σ sensitivity for 1 hr integration time in band 6 (211–275 GHz) will be 42 μ Jy (de Ugarte Postigo et al. 2011b). Thus ALMA should be able to detect all mm afterglows for $n > 0.1$ cm $^{-3}$. Not only is the mm/submm flux density brighter than the cm emission, it does not suffer from diffractive and refractive interstellar scintillation.

To determine the dependence of radio afterglow brightness as a function of ϵ_B , we plot the lightcurves for various values of fractional magnetic energy density in the top right plot of Figure 26. We derive the light curves for a burst at a $z = 3$ and for circumburst density $n = 10$ cm $^{-3}$. Here again we fix the rest of the parameters as above. We note that higher the magnetic energy density, the brighter the radio afterglow during its full evolution. Again this is in contrast to radio light curves at 8 GHz (§6), where higher ϵ_B was suppressing the optically thick flux density in high density medium.

As expected, the mm afterglow strength also very strongly depends upon the kinetic energy of the burst (lower left panel of Figure 26). ALMA will have some difficulties detecting a burst with $E_{KE,iso} < 10^{52}$. In the lower right panel of the Figure 26, we determine the redshift dependence of radio afterglows for values of $z = 0.5, 1, 3, 5$ and 8 . Here we again fix other parameters as $E_{KE,iso} = 10^{53}$ erg, $\theta_j = 0.2$ rad, $\epsilon_e = 0.1$, $\epsilon_B = 1\%$, $n = 10$ cm $^{-3}$, and $p = 2.2$. The trend is similar to the cm but the mm/submm lacks the synchrotron self-absorption contribution to the negative- k correction.

8. DISCUSSION AND CONCLUSIONS

In this paper we have formed a radio-selected sample of 304 GRBs based on 14 years of observations. In addition to the radio observations, we have collected supplementary data including redshift, gamma-ray fluence, and optical and X-ray flux densities on all bursts. We have used these data to carry out the first comparative and correlative study of the prompt and afterglow emission across the full electromagnetic spectrum. Previous studies (e.g. Gehrels et al. 2008; Nysewander et al. 2009; Kann et al. 2010) have not included radio data in the analysis.

We show that the fractional detection rate of radio afterglows is 31% (§2.2). These detection statistics do not change substantially between the pre-*Swift* (42/123 or 34%) and post-*Swift* (53/181 or 29%) samples. This is markedly different than the factor of two increase in the detection probability of optical and X-ray afterglows post-*Swift*. The benefits of *Swift*’s on-board detection, autonomous slews, and the availability of rapid, well-localized positions are not realized by the slower evolving radio afterglows.

Next we investigated the flux density distribution of the radio afterglows for cosmological GRBs (§3.5). The mean flux density in the 8.5 GHz band between days 2–8 of the 65 detections is 287 ± 26 μ Jy. But if we include the non-detections (i.e. total of 157 8.5 GHz flux density points between days 2–8), using a Kaplan-Meier estimator, the mean is 162 ± 15 μ Jy. We also showed

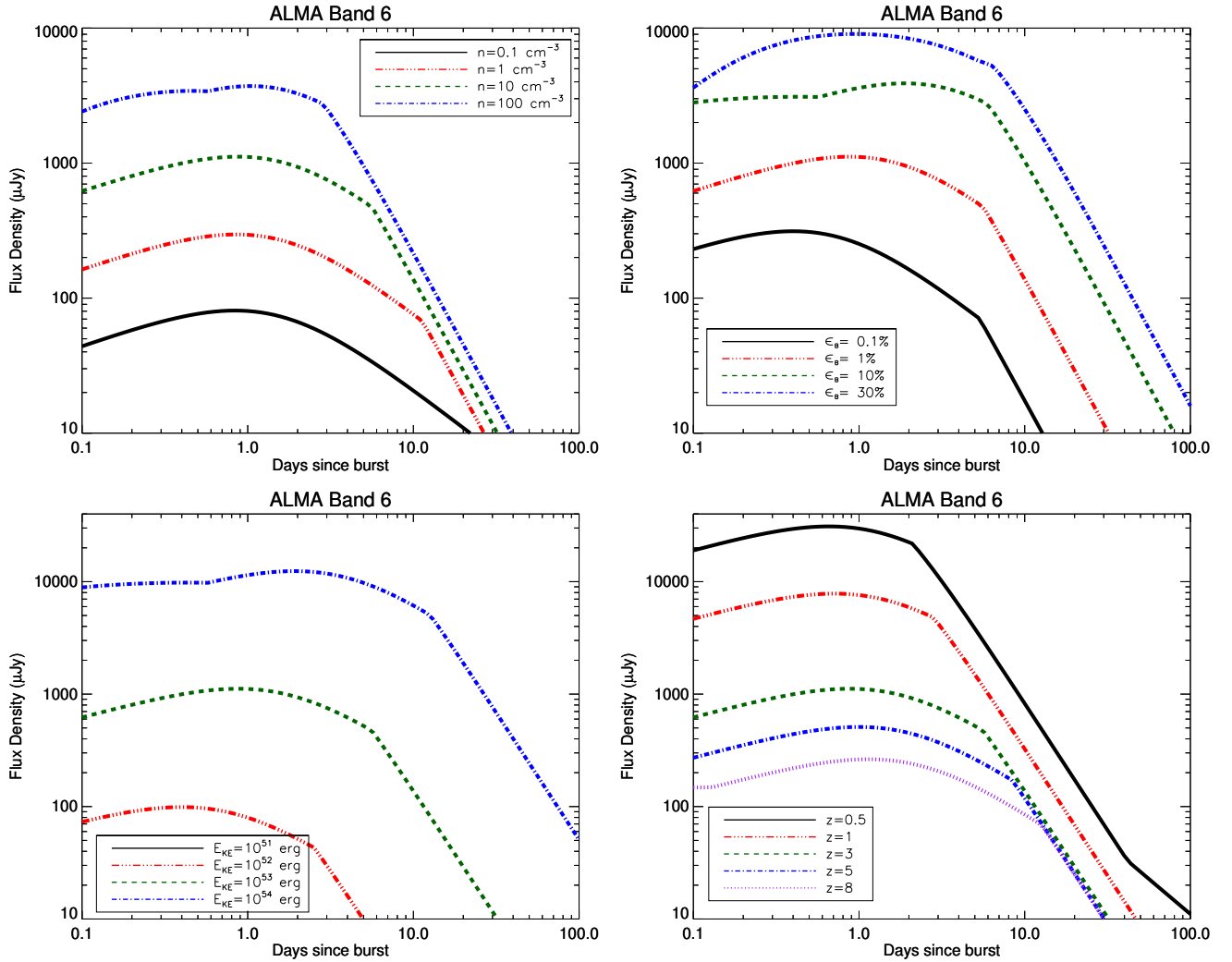


Figure 26. ALMA 250 GHz (Band 6) synthetic light curves for various values of density (top left), magnetic energy density (top right), isotropic kinetic energy (lower left) and redshift (lower right). ALMA band 6 sensitivity in its full capability will be $42 \mu\text{Jy}$ in 1 hr integration time.

that range between the peak flux density of the brightest afterglow and the faintest afterglow spans only a narrow range (a factor of 50), in sharp contrast to optical and X-ray afterglows which range over several orders of magnitude. Together this suggests that the radio afterglow searches are sensitivity limited and that this bias will be present in correlative studies (see below).

Using the measured redshifts for our sample, we calculated the mean spectral luminosity and the mean time-to-peak to be $\sim 10^{31} \text{ erg s}^{-1} \text{ Hz}^{-1}$ and 3-6 days, respectively (§3.5). We investigated the luminosity distribution of several sub-classes of GRBs including the long-duration, cosmological GRBs (LGRB), short-hard bursts (SHB), X-ray flashes (XRF) and GRBs with firm supernova associations (SNe/GRB). There are a wide spread of luminosities for these different subclasses with LGRBs the brightest on average, while SHBs are nearly two orders of magnitude fainter than LGRBs, and XRFs and SNe/GRBs are ten times fainter than LGRBs, albeit with large scatter (§3.4). The best sampled radio light curves are those of the LGRB class with multiple data points that range from nearly 0.01 d to 1000 d. The canonical LGRB will reach a peak luminosity

of $\sim 2 \times 10^{31} \text{ erg s}^{-1} \text{ Hz}^{-1}$ about 3 to 6 days in the rest frame, and after about 10 to 20 days will undergo a power law decline with an index of order unity (§3.3). There is some (not strong) evidence of two equally luminous emission components with a transition occurring at 1 d in the rest frame. The early component may be the result of the reverse shock as has been claimed previously for several bursts (Kulkarni et al. 1999; Fox et al. 2003; Berger et al. 2003b; Chandra et al. 2010) while the later component is the standard forward shock which has been studied through extensive broad-band modeling (Panaitescu & Kumar 2001).

Before any correlative analysis was carried out, we investigated the high energy and non-radio afterglow properties for our sample. We find that the distribution of gamma-ray fluence, duration, energy, and optical/X-ray flux densities for the 304 GRBs in our sample are not dissimilar those from previous studies. There is a difference in the redshift distribution (§4.1). While the mean redshift for our pre-*Swift* sample agrees with past work, for our post-*Swift* sample we derive a lower value for the mean redshift (2.0) based on the radio selected sample compared to published values of $z = 2.2$

(Fynbo et al. 2009) and $z = 2.8$ (Jakobsson et al. 2006), with Fynbo et al. (2009) value closer to our mean. Owing to a negative k -correction (Ciardi & Loeb 2000), radio afterglows are rather insensitive to redshift but we show that the mean radio flux density of high redshift GRBs are close to the sensitivity limit of a typical observation made with existing instruments. This bias will have an effect on any distance-dependent correlations.

We examined the observed GRB and afterglow parameters for the radio sample (§4) and we found that radio-detected GRBs had higher fluences, larger energies, and brighter X-ray and optical fluxes on average, compared to radio non-detections. There is evidently a statistical relationship between the detectability of a radio afterglow and these properties. Further correlations were explored between the peak radio flux density and gamma-ray fluence, optical flux density and X-ray flux density (§5). The only significant correlation that was found was between the peak radio flux density and the optical flux density at 11 hr.

The synthetic light curves §6 show that EVLA Ka band (26-40 GHz) and ALMA mm/submm bands are the most favorable bands for radio afterglow studies. We also show that the centimeter radio afterglow emission will be brightest for circumburst densities between $n = 1 - 10 \text{ cm}^{-3}$. Outside of this range, the flux density will be weak either due to a low intrinsic emission strength (at lower densities) or due to increased synchrotron self-absorption (at higher densities). Within this density range there is a simple relationship of increasing strength of the centimeter radio emission and the fraction of the shock energy in the magnetic field (ϵ_B), but at higher densities synchrotron absorption suppresses the emission. The synthetic light curves also confirm what is already well-established and that is that the radio afterglow flux density is only weakly dependent on redshift at $z \geq 2.5$.

We also make predictions at mm/submm wavelengths (§7), showing that ALMA should be able to detect most afterglows assuming typical parameters. The synchrotron self absorption effect does not play a major role in the mm/submm bands, thus ALMA should be able to detect afterglows very early on. ALMA should be able to provide a true distribution of the mm/submm afterglows, which is not well known. With an order of magnitude of continuum sensitivity of the EVLA and two orders of magnitude sensitivity of the ALMA, EVLA and ALMA will dominate GRB afterglow studies in the future. These telescopes will increase the temporal phase space and the redshift space over which GRBs can be observed. We illustrate this in Figure 25 with the EVLA $3\text{-}\sigma$ spectral luminosity sensitivity at redshifts of 1, 3 and 8.

We thank the anonymous referee for helpful comments. We thank all our numerous colleagues over the last 15 years who took the original data upon which this paper is based. Special mention is due to Shri Kulkarni, Edo Berger, Alicia Soderberg, Brian Cameron, Josh Bloom, Brian Metzger, and Brad Cenko for their roles in the VLA program, Mark Wieringa for the ATCA data and Guy Pooley for the Ryle telescope data. We thank David Alexander Kann, Bing Zhang, Neil Gehrels and Alexander J. van der Horst for useful

suggestions. We acknowledge the frequent use of GRBlog (<http://grblog.org/grblog.php>), GCN circulars (http://gcn.gsfc.nasa.gov/gcn3_archive.html), Nat Butler's Swift BAT+XRT(+optical) lightcurve repository (<http://astro.berkeley.edu/~nat/swift/>) and Jochen Greiner's GRB afterglow page (<http://www.mpe.mpg.de/~jcjg/grb.html>). We also thank online Swift/XRT GRB lightcurve repository http://www.swift.ac.uk/xrt_curves/. The National Radio Astronomy Observatory is a facility of the National Science Foundation operated under cooperative agreement by Associated Universities, Inc. This research has made use of the GHostS database (www.grbhosts.org), which is partly funded by Spitzer/NASA grant RSA Agreement No. 1287913. P.C. is supported by her NSERC Discovery grants as well as the DND-ARP grants held by Kristine Spekkens and Gregg Wade at the Royal Military College of Canada.

REFERENCES

- Aleksić, J., Anderhub, H., Antonelli, L. A., et al. 2010, *A&A*, 517, A5
- Amati, L. 2006, *MNRAS*, 372, 233
- Andersen, M. L., Hjorth, J., Pedersen, H., et al. 2000, *A&A*, 364, L54
- Antonelli, L. A., Piro, L., Vietri, M., et al. 2000, *ApJ*, 545, L39
- Band, D., Matteson, J., and Ford, L., et al. 1993, *ApJ*, 413, 281
- Berger, E., Shin, M.-S., Mulchaey, J. S., & Jeltama, T. E. 2007, *ApJ*, 660, 496
- Berger, E., Price, P. A., Cenko, S. B., et al. 2005a, *Nature*, 438, 988
- Berger, E., Kulkarni, S. R., Fox, D. B., et al. 2005b, *ApJ*, 634, 501
- Berger, E. 2004a, Third Rome Workshop on Gamma-Ray Bursts in the Afterglow Era ASP Conference Series, Rome, Italy, 17-20 September 2002, Volume 312, Eds: Feroci, F. Frontera, N. Masetti, and L. Piro. San Francisco: Astronomical Society of the Pacific, 2004., p.163
- Berger, E., Kulkarni, S. R., & Frail, D. A. 2004b, *ApJ*, 612, 966
- Berger, E., Kulkarni, S. R., Pooley, G., et al. 2003a, *Nature*, 426, 154
- Berger, E., Soderberg, A. M., Frail, D. A., & Kulkarni, S. R. 2003b, *ApJ*, 587, L5
- Bloom, J. S., Frail, D. A., & Kulkarni, S. R. 2003, *ApJ*, 594, 674
- Bloom, J. S., Frail, D. A., & Sari, R. 2001, *AJ*, 121, 2879
- Bradt, H., Levine, A. M., Marshall, F. E., et al. 2001, Gamma-ray Bursts in the Afterglow Era, Rome, Italy, 17-20 October 2000, ESO Astrophysics Symposia. ISBN 3-540-42771-6. Eds: Costa, F. Frontera, and J. Hjorth. Springer-Verlag, 2001, p. 26
- Bremer, M., Krichbaum, T. P., Galama, T. J., et al. 1998, *A&A*, 332, L13
- Butler, N. R., Kocevski, D., Bloom, J. S., & Curtis, J. L. 2007, *ApJ*, 671, 656
- Cardone, V. F., Capozziello, S., & Dainotti, M. G. 2009, *MNRAS*, 400, 775
- Castro-Tirado, A. J., de Ugarte Postigo, A., Gorosabel, J., et al. 2008, *Nature*, 455, 506
- Cenko, S. B., Frail, D. A., Harrison, F. A., et al. 2011, *ApJ*, 732, 29
- Cenko, S. B., Kasliwal, M., Harrison, F. A., et al. 2006, *ApJ*, 652, 490
- Chandra, P., Frail, D. A., Fox, D., et al. 2010, *ApJ*, 712, L31
- Chandra, P., Cenko, S. B., Frail, D. A., et al. 2008, *ApJ*, 683, 924
- Christensen, L., Hjorth, J., & Gorosabel, J. 2005, *ApJ*, 631, L29
- Chornock, R., Berger, E., Fox, D., et al. 2010, GRB Coordinates Network, 11164
- Ciardi, B., & Loeb, A. 2000, *ApJ*, 540, 687
- Connaughton, V., Kippen, R. M., Preece, R., et al. 1997, *IAU Circ.*, 6683
- Costa, E., Frontera, F., Heise, J., et al. 1997, *Nature*, 387, 783
- Cucchiara, A., Levan, A. J., Fox, D. B., et al. 2011, *ApJ*, 736, 7

- Dado, S., & Dar, A. 2010, *ApJ*, 708, L112
- de Pasquale, M., Piro, L., Gendre, B., et al. 2006, *A&A*, 455, 813
- de Ugarte Postigo, A., & the X-shooter GRB collaboration 2011a, *Astronomische Nachrichten*, 332, 297
- Postigo, A. de Ugarte, Lundgren, A., Martin, S., et al. 2011b, arXiv/1108.1797
- Evans, P. A., et al. 2009, *MNRAS*, 397, 1177
- Evans, P. A., Beardmore, A. P., Page, K. L., et al. 2007, *A&A*, 469, 379
- Feigelson, E. D., Nelson, P. I. 1985, *ApJ*, 293, 192
- Firmani, C., Ghisellini, G., Avila-Reese, V., & Ghirlanda, G. 2006, *MNRAS*, 370, 185
- Fox, D. W., Price, P. A., Soderberg, A. M., et al. 2003, *ApJ*, 586, L5
- Frail, D. A., Cameron, P. B., Kasliwal, M., et al. 2006, *ApJ*, 646, L99
- Frail, D. A. 2005, *IAU Colloq. 192: Cosmic Explosions, On the 10th Anniversary of SN1993J*, Eds: Marcaide, J. M. & Weiler, K. W. *Springer Proceedings in Physics*, vol. 99. Berlin: Springer, 2005, 451
- Frail, D. A., Kulkarni, S. R., Berger, E., & Wieringa, M. H. 2003, *AJ*, 125, 2299
- Frail, D. A., Kulkarni, S. R., Sari, R., et al. 2001, *ApJ*, 562, L55
- Frail, D. A., Waxman, E., & Kulkarni, S. R. 2000, *ApJ*, 537, 191
- Frail, D. A., Kulkarni, S. R., Nicastro, L., et al. 1997, *Nature*, 389, 261
- Frontera, F., Guidorzi, C., Montanari, E., et al. 2009, *ApJS*, 180, 192
- Fynbo, J. P. U., Jakobsson, P., Prochaska, J. X., et al. 2009, *ApJS*, 185, 526
- Gandolfi, G., Coletta, A., Ricci, D., et al. 1999, *IAU Circ.*, 7174
- Gehrels, N., Ramirez-Ruiz, E., & Fox, D. B. 2009, *ARA&A*, 47, 567
- Gehrels, N., Barthelmy, S. D., Burrows, D. N., et al. 2008, *ApJ*, 689, 1161
- Ghirlanda, G., Ghisellini, G., & Lazzati, D. 2004, *ApJ*, 616, 331
- Ghirlanda, G., Nava, L., & Ghisellini, G. 2010, *A&A*, 511, A43
- Gorosabel, J., Fynbo, J. P. U., Fruchter, A., et al. 2005, *A&A*, 437, 411
- Graham, J. F., Fruchter, A. S., Levan, A. J., et al. 2009, *ApJ*, 698, 1620
- Greiner, J., Klose, S., Salvato, M., et al. 2003, *ApJ*, 599, 1223
- Hjorth, J., & Bloom, J. S. 2011, arXiv:1104.2274
- Jakobsson, P., et al. 2006, *A&A*, 447, 897
- Jakobsson, P., Hjorth, J., Fynbo, J. P. U., et al. 2004, *ApJ*, 617, L21
- Kann, D. A., Klose, S., Zhang, B., et al. 2011, *ApJ*, 734, 96
- Kann, D. A., Klose, S., Zhang, B., et al. 2010, *ApJ*, 720, 1513
- Kann, D. A., Klose, S., & Zeh, A. 2006, *ApJ*, 641, 993
- Kasliwal, M. M., Cenko, S. B., Kulkarni, S. R., et al. 2008, *ApJ*, 678, 1127
- Koshut, T. M., Paciesas, W. S., Kouveliotou, C., et al. 1995, *Bulletin of the American Astronomical Society*, 27, 886
- Kouveliotou, C., Meegan, C. A., Fishman, G. J., Bhat, N. P., Briggs, M. S., Koshut, T. M., Paciesas, W. S., & Pendleton, G. N. 1993, *ApJ*, 413, L101
- Kuin, N. P. M., Landsman, W., Page, M. J., et al. 2009, *MNRAS*, 395, L21
- Kulkarni, S. R., Frail, D. A., Sari, R., et al. 1999, *ApJ*, 522, L97
- Lazzati, D., Ghisellini, G., Amati, L., et al. 2001, *ApJ*, 556, 471
- Liang, E.-W., Zhang, B.-B., & Zhang, B. 2007, *ApJ*, 670, 565
- Liang, E., & Zhang, B. 2006, *ApJ*, 638, L67
- McBreen, S., Krühler, T., Rau, A., et al. 2010, *A&A*, 516, A71
- Melandri, A., Mundell, C. G., Kobayashi, S., et al. 2008, *ApJ*, 686, 1209
- Nardini, M., Ghisellini, G., Ghirlanda, G., et al. 2006, *A&A*, 451, 821
- Nousek, J. A., et al. 2006, *ApJ*, 642, 389
- Nysewander, M., Fruchter, A. S., & Pe'er, A. 2009, *ApJ*, 701, 824
- Oates, S. R., et al. 2011, *MNRAS*, 412, 561
- Oates, S. R., Page, M. J., Schady, P., et al. 2009, *MNRAS*, 395, 490
- O'Meara, J., Chen, H.-W., & Prochaska, J. X. 2010, GRB Coordinates Network, 11089
- Panaitescu, A., & Kumar, P. 2001, *ApJ*, 560, L49
- Pandey, S. B., Swenson, C. A., Perley, D. A., et al. 2010, *ApJ*, 714, 799
- Pélangeon, A., Atteia, J. -L.; Nakagawa, Y. E., et al. 2008, *A&A*, 491, 157
- Pian, E., Mazzali, P. A., Masetti, N., et al. 2006, *Nature*, 442, 1011
- Press, W. H. et al. 1992, *Numerical Recipes in C* (Cambridge: Cambridge Univ. Press)
- Racusin, J. L., et al. 2011, *ApJ*, 738, 138
- Racusin, J. L., Liang, E. W.; Burrows, D. N., et al. 2009, *ApJ*, 698, 43
- Rao, A. R., Malkar, J. P., Hingar, M. K., et al. 2011, *ApJ*, 728, 42
- Rol, E., Wijers, R. A. M. J., Kouveliotou, C., Kaper, L., & Kaneko, Y. 2005, *ApJ*, 624, 868
- Roming, P. W. A., Koch, T. S., Oates, S. R., et al. 2009, *ApJ*, 690, 163
- Sakamoto, T., Barthelmy, S. D., Baumgartner, W. H., et al. 2011, *ApJS*, 195, 2
- Sakamoto, T., Barthelmy, S. D., Barbier, L., et al. 2008, *ApJS*, 175, 179
- Sakamoto, T., Lamb, D. Q., Kawai, N., et al. 2005, *ApJ*, 629, 311
- Salvaterra, R., Della Valle, M., Campana, S., et al. 2009, *Nature*, 461, 1258
- Sazonov, S. Y., Lutovinov, A. A., & Sunyaev, R. A. 2004, *Nature*, 430, 646
- Schlegel, D. J., Finkbeiner, D. P., & Davis, M. 1998, *ApJ*, 500, 525
- Schulze, S., Klose, S., Björnsson, G., et al. 2011, *A&A*, 526, A23
- Shepherd, D. S., Frail, D. A., Kulkarni, S. R., & Metzger, M. R. 1998, *ApJ*, 497, 859
- Smith, I. A., Tilanus, R. P. J., Tanvir, N., et al. 2005, *A&A*, 439, 987
- Smith, I. A., Tilanus, R. P. J., van Paradijs, J., et al. 1999, *A&A*, 347, 92
- Smith, I. A., Gruendl, R. A., Liang, E. P., & Lo, K. Y. 1997a, *ApJ*, 487, L5
- Smith, D. A., Levine, A. M., Morgan, E. H., & Wood, A. 1997b, *IAU Circ.*, 6718
- Soderberg, A. M., Kulkarni, S. R., Nakar, E., et al. 2006a, *Nature*, 442, 1014
- Soderberg, A. M., Berger, E., Kasliwal, M., et al. 2006b, *ApJ*, 650, 261
- Soderberg, A. M., Kulkarni, S. R., Fox, D. B., et al. 2005, *ApJ*, 627, 877
- Soderberg, A. M., Kulkarni, S. R., Berger, E., et al. 2004, *Nature*, 430, 648
- Spergel, D. N., Bean, R., Doré, O., et al. 2007, *ApJS*, 170, 377
- Starling, R. L. C., Wijers, R. A. M. J., Wiersema, K., Rol, E., et al. 2007, *ApJ*, 661, 787
- Tanvir, N. R., Rol, E., Levan, A. J., et al. 2010a, *ApJ*, 725, 625
- Tanvir, N. R., Wiersema, K., & Levan, A. J. 2010b, GRB Coordinates Network, 11230
- Tanvir, N. R., Fox, D. B., Levan, A. J., et al. 2009, *Nature*, 461, 1254
- Tinney, C., Stathakis, R., Cannon, R., & Galama, T. 1998, *IAU Circ.*, 6896
- Yonetoku, D., Murakami, T., Nakamura, T., et al. 2004, *ApJ*, 609, 935
- Yost, S. A., Harrison, F. A., Sari, R., & Frail, D. A. 2003, *ApJ*, 597, 459
- van der Horst, A. J., Kamble, A., Resmi, L., et al. 2008, *A&A*, 480, 35
- van Paradijs, J., et al. 1997, *Nature*, 386, 686
- Zhang, B., Fan, Y. Z., Dyks, J., et al. 2006, *ApJ*, 642, 354

Table 6
Master table

1	2	3	4	5	6	7	8	9	10	11	12	13	14	15	16	17	18	19
GRB	Inst. ^a	RA J2000	Decl. J2000	X ^b	O ^c	R ^d	Radio Tel	T ₉₀ s	z	S _{15–150} ^e erg cm ⁻²	E _{iso} ^{bol f} erg	F _X ^{11h g} CGS	F _R ^{11h h} μJy	t _j d	n _i ⁱ cm ⁻³	θ _j deg.	E _{true} ^{bol j} erg	References ^k
970111	B, T	15:28:15.0	+19:36:18	N	N	N	VLA ^r	31	...	3.30E-05	19, [], [], [], [], [], []
970228 ⁿ	B	05:01:46.7	+11:46:53	Y	Y	N	VLA	56	0.695	5.55E-06	1.60E+52	20.8	22.0	19, [], [], [], [], [], []
970402	B	14:50:06.0	-69:20:00	Y	N	N	ATCA	105	...	4.84E-06	...	1.4	19, [], [], [], [], [], []
970508	B	06:53:49.2	+79:16:19	Y	Y	Y	VLA ^r	14	0.835	1.11E-06	7.10E+51	5.7	6.5	25	1	20.93	4.74E+50	19, [], [], [], [], [], []
970616	B, T	01:18:48.0	-05:26:18	Y	N	N	VLA	200	...	1.78E-05	...	38.6	28, [], [], [], [], [], []
970815	A	16:06:54.0	+81:30:34	Y	Y	N	VLA	130	...	8.66E-06	29, [], [], [], [], [], []
970828	A	18:08:31.7	+59:18:50	Y	N	Y	VLA	147	0.958	1.16E-04	2.96E+53	19.9	...	2.2	[1]	5.15	1.20E+51	20, [], [], [], [], [], []
971214	B	11:56:26.4	+65:12:01	Y	Y	N	VLA	35	3.420	4.35E-06	2.11E+53	6.4	5.6	>2.5	[1]	>4.15	>5.55E+50	20, [], [], [], [], [], []
971227	B	12:57:15.0	+59:24:02	Y	N	N	VLA	7	...	4.42E-07	...	4.0	13, [], [], [], [], [], []
980109	B	00:25:56.0	-63:01:24	X	N	N	ATCA	20	...	1.91E-06	13, [], [], [], [], [], []
980326 ⁿ	B	08:36:34.3	-18:51:24	X	Y	N	VLA	9	0.9-1.1	5.03E-07	5.60E+51	...	11.9	<0.4	[1]	<4.43	<1.67E+49	13, 53, [], [], [], [], []
980329	B	07:02:38.0	+38:50:44	Y	Y	Y	VLA	58	2-3.9	4.36E-05	2.10E+54	6.0	2.3	<1	20	<3.34	<3.56E+51	13, 53, [], [], [], [], []
980425 ⁿ	B	19:35:03.2	-52:50:46	Y	Y	Y	ATCA	31	0.009	1.91E-06	1.60E+48	2.8	<24.6	...	[1]	13, 7, [], [], [], [], []
980515	B	21:16:49.0	-67:11:48	Y	N	N	ATCA	15	...	1.54E-06	...	5.6	13, [], [], [], [], [], []
980519	B	23:22:21.5	+77:15:43	Y	Y	Y	VLA	30	...	5.43E-06	...	3.9	62.4	0.55	0.14	13, [], [], [], [], [], []
980613	B	10:17:57.8	+71:27:26	Y	Y	N	VLA	50	1.097	6.63E-07	6.90E+51	2.6	2.9	>3.1	[1]	>9.13	>8.77E+49	13, 7, [], [], [], [], []
980703	A	23:59:06.7	+08:35:07	Y	Y	Y	VLA ^s	90	0.966	2.01E-05	6.90E+52	14.0	35.5	7.5	28	14.82	2.31E+51	13, 7, [], [], [], [], []
981220	A, T	03:42:33.7	+17:09:00	X	N	N	VLA ^{r, s}	15	...	6.70E-06	26, [], [], [], [], [], []
981226	B	23:29:37.2	-23:55:54	Y	N	Y	VLA ^r	20	1.11	2.68E-07	5.9E+51	2.8	...	>5	[1]	>11.12	>1.11E+50	13, 67, [], [], [], [], []
990123	B	15:25:30.3	+44:45:59	Y	Y	Y	VLA ^{r, t}	100	1.600	1.20E-04	2.39E+54	54.2	37.8	2.04	[1]	3.47	4.38E+51	20, 33, [], [], [], [], []
990217	B	03:02:52.3	-53:05:37	N	N	N	ATCA	25	...	8.51E-07	13, [], [], [], [], [], []
990308	A, T	12:23:11.4	+06:44:05	X	Y	N	VLA	0.5	...	3.50E-06	65.8	26, [], [], [], [], [], []
990506	P, T	11:54:50.1	-26:40:35	Y	N	Y	VLA	220	1.307	5.65E-05	9.49E+53	42.5	20, 14, [], [], [], [], []
990510	B	13:38:07.1	-80:29:48	Y	Y	Y	ATCA	75	1.169	1.21E-05	1.78E+53	34.7	181.9	1.2	0.29	3.36	3.06E+50	20, 7, [], [], [], [], []
990520	B	08:35:56.0	+51:18:36	X	N	N	VLA	10	...	5.29E-07	30, [], [], [], [], [], []
990627	B	01:48:25.4	-77:04:38	Y	N	N	ATCA	59	...	2.06E-06	...	0.3	19, [], [], [], [], [], []
990704	B	12:19:27.3	-03:50:22	Y	N	N	VLA ^r	23	...	6.70E-07	...	5.9	20, [], [], [], [], [], []
990705	B	05:09:54.5	-72:07:53	Y	Y	N	ATCA	42	0.840	2.83E-04	1.82E+53	1.9	13.0	1	[1]	4.17	4.82E+50	20, 9, [], [], [], [], []
990712 ⁿ	B	22:31:53.0	-73:24:28	X	Y	N	ATCA	30	0.433	4.36E-06	6.72E+51	...	26.2	>47.7	[1]	>29.46	>8.89E+50	13, 14, [], [], [], [], []
991014	B	06:51:03.0	+11:36:05	Y	N	N	VLA	3	...	6.03E-07	...	5.4	13, [], [], [], [], [], []
991106	B	22:24:40.8	+54:22:45	Y	N	N	VLA	3.04E-06	...	1.3	[], [], [], [], [], []
991208 ⁿ	T	16:33:53.5	+46:27:21	X	Y	Y	VLA ^{r, s, t}	60	0.706	8.09E-05	1.10E+53	...	392.5	<2.1	18	<8.66	<1.26E+51	26, [], [], [], [], [], []
991216	P	05:09:31.3	+11:17:07	Y	Y	Y	VLA ^{r, s, t}	25	1.020	6.50E-05	6.75E+53	78.1	571.1	1.2	4.7	4.44	2.03E+51	20, 33, [], [], [], [], []
000115	P, T	08:03:30.0	-17:13:30	Y	N	N	VLA	15	...	1.37E-05	...	53.0	26, [], [], [], [], [], []
000126	T	07:45:00.0	+07:44:30	X	N	N	VLA	70	...	1.65E-05	26, [], [], [], [], [], []
000131	T	06:13:31.0	-51:56:40	X	Y	Y	ATCA	110	4.500	1.65E-05	1.84E+54	...	10.2	>3.5	[1]	<3.31	<3.07E+51	20, 33, [], [], [], [], []
000210	B	01:59:15.6	-40:39:33	Y	N	Y	VLA ^u	10	0.850	4.09E-05	2.00E+53	3.1	...	>1.7	[1]	>5.02	>7.67E+50	13, 9, [], [], [], [], []
000214	B	18:54:27.0	-66:27:30	Y	N	N	ATCA	115	0.470	4.13E-06	8.00E+51	6.2	13, 4, [], [], [], [], []
000226	T	21:28:57.8	-19:45:42	X	X	N	VLA	131	...	3.30E-05	26, [], [], [], [], [], []
000301A	T	23:39:27.1	+75:47:13	X	X	N	VLA ^r	6	...	3.30E-06	26, [], [], [], [], [], []
000301C	T	16:20:18.6	+29:26:36	X	Y	Y	VLA ^t	10	2.034	3.47E-06	4.37E+52	...	66.3	5.5	25	11.71	9.12E+50	26, 7, [], [], [], [], []
000315	T	22:43:20.6	+17:59:36	X	X	N	VLA	60	...	6.60E-05	26, [], [], [], [], [], []
000326	T	22:11:23.5	-26:08:46	X	N	N	VLA	2	...	4.95E-06	26, [], [], [], [], [], []
000418	T	12:25:19.3	+20:06:11	X	Y	Y	VLA ^t	30	1.119	2.15E-05	7.51E+52	...	32.1	25	27	22.30	5.69E+51	26, 7, [], [], [], [], []
000424	B	06:58:52.3	+49:52:23	X	N	N	VLA	1.85E-06	[], [], [], [], [], []
000519	T	23:04:38.6	+01:10:17	X	N	N	VLA	15	...	3.20E-06	26, [], [], [], [], [], []
000528	B	10:45:08.0	-33:59:26	Y	N	N	VLA	80	...	9.65E-07	...	3.0	13, [], [], [], [], [], []
000529	B	00:09:48.3	-61:27:53	Y	N	N	ATCA	4	...	1.54E-07	...	1.6	19, [], [], [], [], [], []
000604	T	15:35:47.2	+10:41:18	X	N	N	VLA	15	...	2.15E-05	26, [], [], [], [], [], []
000607	T	02:33:58.7	+17:08:51	X	N	N	VLA	0.2	...	3.30E-07	13, [], [], [], [], [], []
000615A	B	15:32:40.3	+73:50:53	N	N	N	VLA	12	...	6.57E-07	26, [], [], [], [], [], []
000620	B	07:35:17.2	+69:11:35	X	N	N	VLA	15	...	1.12E-06	13, [], [], [], [], [], []
000630	T	14:47:13.5	+41:13:53	X	Y	N	VLA	20	...	3.30E-06	3.3	>4	[1]	26, [], [], [], [], [], []
000727	T	11:45:10.5	+17:24:34	X	N	N	VLA	10	...	4.29E-06	26, [], [], [], [], [], []
000801	T	11:11:46.1	-09:24:44	X	N	N	VLA	30	...	2.81E-05	26, [], [], [], [], [], []
000812	T	18:08:43.7	+45:50:47	X	N	N	VLA	80	...	3.30E-05	26, [], [], [], [], [], []
000830	T	23:34:12.1	+06:20:47	X	N	N	VLA	9	...	8.58E-06	26, [], [], [], [], [], []
000911 ⁿ	T	02:18:34.4	+07:44:29	X	Y	Y	VLA	500	1.059	8.25E-06	8.80E+53	...	57.3	<1.5	[1]	<3.82	<1.96E+51	20, 33, [], [], [], [], []
000926	T	17:04:09.7	+51:47:10	X	Y	Y	VLA ^t	25	2.039	3.63E-05	2.70E+53	...	105.4	1.8	27	6.19	1.58E+51	26, 33, [], [], [], [], []
001007	T	04:05:54.3	-21:53:46	X	Y	Y	VLA	375	...	5.45E-05	139.5	56, [], [], [], [], [], []
001018	T	13:14:10.3	+11:48:32	X	X	Y	VLA	31	...	1.98E-05	56, [], [], [], [], [], []
001025B ^o	T	18:21:40.8	-05:08:34	X	N	N	VLA	0.3	...	3.30E-07	56, [], [], [], [], [], []
001109	B	18:30:07.8	+55:17:56	Y	N	N	VLA ^r	60	...	8.20E-06	...	23.2	13, [], [], [], [], [], []
001204 ^o	T	02:41:08.6	+12:53:46	X	N	N	VLA	0.5	...	1.42E-06	56, [], [], [], [], [], []
010119 ^o	T	18:53:49.5	+12:01:13	X	N	N	VLA	0.2	...	5.28E-07	26, [], [], [], [], [], []
010213 ^p	H	10:31:36.0	+05:30:39	X	N	N	VLA	34	...	4.41E-08	44, [], [], [], [], [], []
010214	B	17:40:58.0	+48:34:37	Y	N	N	VLA	15	...	3.02E-06	...	3.1	13, [], [], [], [], [], []
010220	B	02:36:59.0	+61:46:00	X	N	N	VLA	40	13, [], [], [], [], [], []
010222	B	14:52:12.5	+43:01:06	Y	Y	Y	VLA ^t	170	1.477	5.05E-05	1.33E+54	70.5	76.9	0.93	1.7	3.02	1.85E+51	13, 33, [], [], [], [], []
010728	B	11:40:07.0	-07:56:59	X	X	N	VLA	8	...	8.31E-07	26, [], [], [], [], [], []
010921	H, T	22:55:59.9	+40:55:53	X	Y	Y	VLA	24	0.450	7.12E-06	9.00E+51	...	143.7	33	[1]	24.63	8.32E+50	44, 9, [], [], [], [], []
011030 ^p	B	20:43:35.4	+77:17:20	Y	N	Y	VLA ^{r, t}	...	<3	180.0	[], [], [], [], [], []
011121 ⁿ	B	11:34:29.7	-76:01:42	X	Y	Y	ATCA	105	0.362</									

Table 6 — Continued

1	2	3	4	5	6	7	8	9	10	11	12	13	14	15	16	17	18	19
GRB	Inst. ^a	RA J2000	Decl. J2000	X ^b	O ^c	R ^d	Radio Tel	T ₉₀ s	z	S _{15–150} ^e erg cm ⁻²	E _{iso} ^{bol f} erg	F _X ^{11h g} CGS	F _R ^{11h h} μJy	t _j d	n ⁱ cm ⁻³	θ _j deg.	E _{bol} ^j E _{true} erg	References ^k
050813 ^o	S	16:07:57.00	+11:14:52.0	Y	N	N	VLA	0.5	0.720	4.40E-08	1.50E+50	0.0	45,32,21,8,37,[][],[]
050814	S	17:36:45.39	+46:20:21.6	Y	Y	N	VLA	151	5.300	2.01E-06	6.00E+52	13.8	2.1	1.03	[1]	3.05	8.52E+49	45,37,21,8,37,37,42,[]
050815	S	19:34:23.15	+09:08:47.5	Y	Y	N	VLA	3	...	7.90E-08	...	0.9	45,[]45,[]37,[][],[]
050820A	S, T	22:29:38.11	+19:33:37.1	Y	Y	Y	VLA	240	2.615	3.44E-06	2.00E+53	221.2	87.2	7.35	0.1	5.07	7.82E+50	8,33,21,8,37,21,42,10
050824 ⁿ	S	00:48:56.05	+22:36:28.5	Y	Y	Y	VLA	230	0.830	2.66E-07	1.50E+51	137.7	9.9	45,33,21,8,37,37,[]
050904	S	00:54:50.79	+14:05:09.4	Y	Y	Y	VLA	174	6.290	4.83E-06	1.30E+54	0.5	20.0	...	680	45,33,45,8,37,37,[]18
050906 ^o	S	03:31:11.75	-14:37:18.1	X	N	N	VLA	0.3	...	6.00E-09	45,[]45,[][],[][],[]
050911 ^o	S	00:54:37.70	-38:50:57.7	N	N	N	VLA	16.2	0.165	3.17E-07	2.69E+49	45,6,45,32,[][],[][],[]
050915A	S	05:26:44.80	-28:00:59.3	Y	Y	N	VLA	52	...	8.50E-07	...	5.1	1.0	45,[]21,[]37,37,[][],[]
050922B	S	00:23:13.20	-05:36:16.4	Y	N	N	VLA	151	...	2.23E-06	...	20.0	45,[]45,[]37,[][],[]
050922C	H, S	21:09:33.30	-08:45:27.5	Y	Y	Y	VLA	5	2.199	1.62E-06	3.90E+52	17.2	14.3	45,33,21,8,37,21,[][],[]
051006	S	07:23:13.52	+09:30:24.5	Y	Y	N	VLA	35	...	1.34E-06	...	0.6	11.4	45,[]45,[]37,37,[][],[]
051008	S, T	13:31:29.30	+42:05:59.0	Y	Y	N	VLA	280	...	5.09E-06	...	20.6	0.4	36,[]21,[]37,37,[][],[]
051016A	S	08:11:16.30	-18:17:49.2	Y	N	N	VLA	23	...	8.37E-07	...	3.1	45,[]45,[]37,[][],[]
051016B	S	08:48:27.60	+13:39:25.5	Y	Y	N	VLA	4	0.936	1.70E-07	3.70E+50	15.5	4.9	1.56	[1]	10.49	6.20E+48	36,33,21,8,37,37,42,[]
051021A ^o	H	01:56:36.39	+09:04:03.7	Y	Y	N	VLA	27	...	3.78E-06	...	13.7	6.2	26,[][],[]37,37,[][],[]
051022	H, T	23:56:04.10	+19:36:24.2	Y	Y	Y	VLA ^f	200	0.809	8.25E-05	6.30E+53	426.5	<0.4	26,9,[]3,37,37,[][],[]
051103 ^o	T	09:52:34.08	+68:50:42.0	X	N	N	VLA	0.2	...	8.66E-06	26,[][],[][],[][],[]
051105A ^o	S	17:41:03.28	+34:59:03.6	N	N	N	VLA	0.09	...	2.20E-08	45,[]45,[][],[][],[]
051109A	S, T	22:01:15.31	+40:49:23.3	Y	Y	Y	VLA ^t	37	2.346	2.20E-06	2.30E+52	99.7	39.6	0.92	[1]	4.18	6.13E+49	45,33,21,8,37,21,42,[]
051109B ^p	S	23:01:50.21	+38:40:46.0	Y	N	N	VLA	14	0.080	2.56E-07	3.60E+48	3.9	45,37,45,8,37,[][],[]
051111	S	23:12:33.36	+18:22:29.5	Y	Y	Y	VLA	46	1.550	4.08E-06	6.00E+52	3.4	41.6	45,33,45,8,37,37,[][],[]
051114 ^o	S	15:05:03.84	+60:09:21.6	N	X	N	VLA	1.28E-07	[],[]45,[][],[][],[]
051117A	S	15:13:34.09	+30:52:12.7	Y	Y	N	VLA	136	...	4.34E-06	...	11.3	6.9	45,[]21,[]37,37,[][],[]
051117B	S	05:40:43.00	-19:16:26.5	Y	Y	N	VLA	9	...	1.77E-07	...	0.2	<12.4	45,[]45,[]37,37,[][],[]
051211B	I	23:02:41.57	+55:04:51.5	Y	Y	Y	VLA	80	...	1.90E-06	...	2.9	135.8	55,[][],[]59,37,[][],[]
051221A ^o	S, T	21:54:48.63	+16:53:27.2	Y	Y	Y	VLA ^f	1.4	0.547	1.15E-06	2.80E+51	9.9	7.5	4.07	0.001	5.35	1.22E+49	32,32,21,8,37,37,42,49
051221B	S	20:49:35.10	+53:02:12.2	Y	Y	N	VLA	40	...	9.17E-07	<21.4	45,[]45,[]37,37,[][],[]
051227 ^o	S	08:20:58.11	+31:55:31.9	Y	Y	N	VLA	115	0.714	6.99E-07	8.00E+50	0.9	0.5	45,26,21,8,37,37,[][],[]
060105	S, T	19:50:00.60	+46:20:58.3	Y	N	N	VLA	54	...	1.76E-05	...	37.8	45,[]45,[]37,[][],[]
060108	S	09:48:01.98	+31:55:08.6	Y	Y	N	VLA	14	<2.8	3.69E-07	...	9.8	3.0	36,9,21,[]37,21,[][],[]
060110	S	04:50:57.85	+28:25:55.7	Y	Y	N	VLA	26	...	1.57E-06	...	21.2	59.4	45,[]45,[]37,37,[][],[]
060116	S	05:38:46.28	-05:26:13.1	Y	Y	Y	VLA	106	...	2.41E-06	...	5.8	6.9	45,[]45,[]37,37,[][],[]
060123	S	11:58:47.66	+45:30:50.6	Y	N	N	VLA	900	1.099	3.00E-07	...	27.6	26,26,37,[]37,[][],[]
060124	H, S	05:08:25.50	+69:44:26.0	Y	Y	N	VLA	800	2.297	4.61E-07	7.00E+51	287.3	68.8	0.68	[1]	4.36	2.02E+49	36,33,21,8,37,21,42,[]
060206	S	13:31:43.44	+35:03:03.2	Y	Y	N	VLA ^f	8	4.050	8.31E-07	4.07E+52	20.8	8.2	45,33,21,33,37,21,[][],[]
060210	S	03:50:57.37	+27:01:34.4	Y	Y	N	VLA	255	3.910	7.66E-06	4.20E+53	85.6	13.7	36,33,21,8,37,37,[][],[]
060213	T	09:26:24.14	-09:06:57.4	Y	Y?	N	VLA	60	...	1.60E-04	26,[]37,[][],[][],[]
060218 ^{n,p}	S	03:21:39.68	+16:52:01.8	Y	Y	Y	VLA ^{t,v}	128	0.033	1.57E-06	2.90E+48	48.8	1082.2	>22	5	>80.26	>2.85E+48	8,33,45,8,37,37,50,50
060313 ^o	S, T	04:26:28.40	-10:50:40.1	Y	Y	N	VLA	0.7	...	1.13E-06	...	6.6	9.9	32,[]21,32,37,37,[][],[]
060418	S, T	15:45:42.40	-03:38:22.8	Y	Y	Y	VLA	103	1.490	8.38E-06	1.00E+53	9.4	25.0	45,33,21,8,37,21,[][],[]
060421	S	22:54:32.63	+62:43:50.1	Y	N	N	VLA	12	...	1.25E-06	...	3.9	45,[]45,[]37,[][],[]
060428B ^p	S	15:41:25.63	+62:01:30.3	Y	Y	N	VLA	58	...	8.23E-07	...	3.4	6.3	45,[]21,[]37,37,[][],[]
060502B ^o	S	18:35:45.89	+52:37:56.2	Y	Y	N	VLA	0.13	0.287	4.00E-08	3.00E+49	0.1	<1	45,32,21,8,37,37,[][],[]
060505 ^o	S	22:07:04.50	-27:49:57.8	Y	Y	N	VLA	4	0.089	9.44E-07	4.37E+49	8.1	2.2	32,32,45,32,37,37,[][],[]
060522	S	21:31:44.80	+02:53:10.4	Y	Y	N	VLA	71	5.110	1.14E-06	7.00E+52	3.2	3.7	45,36,45,8,37,37,[][],[]
060604	S	22:28:55.01	-10:54:55.8	Y	Y	N	VLA	95	2.680	4.02E-07	4.37E+51	16.4	17.2	45,9,21,36,37,21,[][],[]
060605	S	21:28:37.32	-06:03:31.3	Y	Y	N	VLA	79	3.773	6.97E-07	2.50E+52	6.1	17.8	0.17	[1]	1.92	1.41E+49	45,33,21,8,37,21,42,[]
060707	S	23:48:19.00	-17:54:17.0	Y	Y	N	VLA	66	3.430	1.60E-06	6.10E+52	25.0	8.1	12.26	[1]	8.80	7.20E+50	45,33,21,8,37,37,42,[]
060719	S	01:13:43.57	-48:22:55.0	Y	Y	N	ATCA	67	<4.6	1.50E-06	...	21.4	<0.1	45,20,21,[]37,37,[][],[]
060801 ^o	S	14:12:01.31	+16:58:54.0	Y	N	N	VLA ^f	0.5	1.131	8.00E-08	3.09E+51	0.1	32,32,21,32,37,37,[][],[]
060825	S	01:12:29.00	+55:47:46.5	Y	N	N	VLA	8	...	9.63E-07	...	3.6	45,[]45,[]37,[][],[]
060908	S, T	02:07:18.36	+00:20:31.2	Y	Y	N	VLA	19	1.884	2.80E-06	7.00E+52	5.9	0.8	36,20,45,8,37,37,[][],[]
060912A	S, T	00:21:08.16	+20:58:17.8	Y	Y	N	VLA	5	0.937	8.69E-07	8.00E+51	4.9	10.3	36,38,45,8,37,37,[][],[]
060923A	S	16:58:28.15	+12:21:38.9	Y	Y	N	VLA	52	...	8.69E-07	...	10.8	0.3	45,[]21,[]37,37,[][],[]
060923C	S	23:04:28.49	+03:55:26.6	Y	Y	N	VLA	76	...	1.58E-06	...	3.6	0.8	45,[]21,[]37,37,[][],[]
060926	S	17:35:43.66	+13:02:18.6	Y	Y	N	VLA	8	3.209	2.19E-07	1.00E+52	2.5	3.3	45,20,45,8,37,37,[][],[]
061028	S	06:28:54.66	+46:17:57.0	Y	N	N	VLA	106	0.760	9.66E-07	2.29E+51	0.8	45,33,45,33,37,[][],[]
061121	S, T	09:48:54.58	-13:11:42.7	Y	Y	Y	VLA ^{f,u}	81	1.315	1.37E-05	1.90E+53	115.1	27.4	36,33,21,8,37,21,[][],[]
061126	S, T	05:46:24.43	+64:12:38.8	Y	Y	N	VLA	71	1.159	6.77E-06	8.00E+52	44.4	8.3	45,33,21,8,37,21,[][],[]
061210 ^o	S	09:38:05.04	+15:36:46.8	Y	N	N	VLA	85	0.410	1.11E-06	9.00E+50	45,32,45,8,[][],[][],[]
061222A	S, T	23:53:03.42	+46:31:58.6	Y	Y	Y	VLA	72	2.088	7.99E-06	1.03E+53	282.1	0.3	0.77	[1]	2.39	1.31E+51	36,57,21,[]37,37,42,[]
061222B	S	07:01:24.60	-25:51:36.0	Y	Y	N	VLA	40	3.355	2.24E-06	8.00E+52	3.1	1.2	45,37,45,8,37,37,[][],[]
070125	T	07:51:17.77	+31:09:04.1	Y	Y	Y	VLA ^{f,v}	60	1.548	6.44E-05	9.55E+53	37.8	207.7	3.8	42	7.90	9.07E+51	26,33,[]33,37,37,11,11
070220	S	02:19:06.83	+68:48:16.1	Y	N	N	VLA	129	...	1.04E-05	...	10.6	45,[]21,[]37,[][],[]
070223	S	10:13:48.39	+43:08:00.7	Y	Y	N	VLA	89	...	1.70E-06	...	6.9	0.6	45,[]21,[]37,37,[][],[]
070306	S	09:52:23.38	+10:28:55.2	Y	Y	N	V											

Table 6 — Continued

1	2	3	4	5	6	7	8	9	10	11	12	13	14	15	16	17	18	19
GRB	Inst. ^a	RA J2000	Decl. J2000	X ^b	O ^c	R ^d	Radio Tel	T ₉₀ s	z	S _{15–150} ^e erg cm ⁻²	E _{iso} ^{bol f} erg	F _X ^{1h g} CGS	F _R ^{1h h} μJy	t _j d	n ⁱ cm ⁻³	θ _j deg.	E _{true} ^{bol j} erg	References ^k
071003	S, T	20:07:24.22	+10:56:50.0	Y	Y	Y	VLA	148	1.604	8.30E-06	3.24E+53	55.7	180.1	46.33, 37.33, 37.37, []
071010A	S	19:12:14.62	-32:24:07.2	Y	Y	N	VLA	6	0.985	2.00E-07	1.32E+51	34.9	43.0	46.33, 37.33, 37.37, []
071010B	S, T	10:02:09.26	+45:43:50.3	Y	Y	Y	VLA	36	0.947	4.40E-06	2.60E+52	45.6	48.3	46.37, 37.46, 37.37, []
071011	S	00:33:32.73	+61:08:04.6	Y	Y	N	VLA	81	...	2.20E-08	...	46.0	26.6	5.49	[1]	46.[] , 37.[] , 37.37, 42.[]
071018	S	10:58:44.40	+53:49:19.2	N	N	N	VLA	288	...	1.00E-06	46.[] , 37.[] , 37.37, []
071020	S, T	07:58:39.78	+32:51:40.4	Y	Y	Y	VLA	4	2.146	2.30E-06	8.91E+52	16.1	13.1	46.33, 37.33, 37.37, []
071021	S	22:42:34.31	+23:43:06.5	Y	Y	Y	VLA	229	<5.6	1.30E-06	...	8.6	1.4	46.[] , 37.[] , 37.37, []
071109	I	19:19:53.90	+02:02:47.5	N	N	Y?	VLA	30	...	6.60E-07	55.[] , 37.[] , 37.37, []
071112B ^o	S	17:20:51.12	-80:53:02.4	N	N	N	ATCA	0.3	...	4.75E-08	32.[] , 46.32, [] , 37.37, []
071112C	S	02:36:50.93	+28:22:16.7	Y	Y	N	VLA ^r	15	0.823	3.00E-06	1.95E+52	3.7	5.6	26.33, 37.33, 37.37, []
071122	S	18:26:25.31	+47:04:30.1	Y	Y	Y	VLA	80	1.140	5.80E-07	3.47E+51	0.5	3.7	46.33, 37.33, 37.37, []
080120	I	15:01:03.28	-10:52:29.8	Y	Y	N	VLA	15	...	1.43E-06	...	0.3	28.2	55.[] , 37.[] , 37.37, []
080212	S	15:24:35.49	-22:44:29.0	Y	Y	N	VLA	117	...	3.05E-06	...	9.1	17.3	46.33, 37.33, 37.37, []
080229	S	15:12:52.39	-14:42:16.8	Y	Y	N	VLA ^u	64	...	9.10E-06	...	6.6	46.[] , 46.[] , 59.[] , 26.[]
080319B ⁿ	S, T	14:31:40.98	+36:18:08.8	Y	Y	Y	VLA ^r	125	0.937	8.50E-05	1.45E+54	49.7	62.9	11.6	[1]	7.91	1.38E+52	46.33, 46.33, [] , 26.52, []
080413A	S, T	19:09:11.75	-27:40:40.0	Y	Y	N	VLA	46	2.433	3.52E-06	1.38E+53	2.2	7.8	46.33, 46.33, [] , 33.[] , []
080413B	S, T	21:44:34.65	-19:58:52.4	Y	Y	N	VLA	8	1.101	3.25E-06	1.59E+52	23.6	62.2	46.32, 46.32, 59.26, []
080430	S	11:01:14.76	+51:41:08.3	Y	Y	N	VLA	14	0.767	1.17E-06	3.00E+51	27.8	17.8	46.1, 46.1, 59.26, []
080503 ^o	S	19:06:28.69	+68:47:37.7	Y	Y	N	VLA	0.3	...	2.00E-06	...	<0.3	0.4	5.27	32.[] , 46.[] , 37.37, []
080506	S	21:57:41.83	+38:59:06.4	Y	Y	N	VLA	152	...	1.29E-06	...	6.4	9.5	1.33	[1]	46.[] , 46.[] , 59.26, 26.[]
080507	sA, T	15:34:43.39	+56:26:08.3	Y	Y	N	VLA	30	...	1.88E-05	...	51.2	8.8	26.[] , 37.[] , 37.37, []
080603A	I	18:37:37.97	+62:44:38.9	Y	Y	Y	VLA	150	1.687	1.05E-06	...	15.8	13.3	55.32, [] , 37.37, []
080603B	S, T	11:46:07.66	+68:03:40.0	Y	Y	N	VLA	59	2.689	2.47E-06	7.70E+52	26.5	44.3	0.004	[1]	0.45	2.39E+48	46.20, 46.26, [] , 26.26, []
080604	S	15:47:51.70	+20:33:28.1	Y	Y	N	VLA	69	1.417	7.89E-07	7.08E+51	2.0	5.4	46.20, 46.8, 59.26, []
080613A	I	14:13:05.31	+05:10:21.2	Y	Y	N	VLA	30	...	1.24E-06	...	10.0	0.9	55.[] , 37.[] , 37.37, []
080702A ^o	S	20:52:12.19	+72:18:45.8	Y	N	N	VLA	0.5	...	3.80E-08	...	2.4	46.[] , 46.[] , 37.37, []
080721	S, T	14:57:55.86	-11:43:24.5	Y	Y	N	VLA	176	2.591	1.41E-05	1.23E+54	61.9	26.7	26.33, 46.33, 59.26, []
080723B	I, sA	11:47:19.96	-60:14:27.5	Y	Y	N	ATCA	95	...	1.24E-05	...	80.1	55.[] , 37.[] , 59.[] , 26.[]
080810	S, T	23:47:10.51	+00:19:11.3	Y	Y	Y	VLA	108	3.350	4.64E-06	5.37E+53	13.4	40.1	46.33, 46.33, 59.33, []
080913	S, T	04:22:54.74	-25:07:46.2	Y	Y	N	VLA	8	6.733	5.71E-07	6.46E+52	0.4	<0.08	46.33, 46.33, [] , 26.[] , []
081024A	S	01:51:29.71	+61:19:53.0	Y	N	N	VLA	2	...	1.27E-07	...	<0.5	46.[] , 46.[] , 59.[] , 26.[]
081024B ^o	F	21:31:36.00	+21:12:14.4	Y	Y?	N	VLA	0.8	...	2.14E-07	26.[] , 37.[] , 37.37, []
081118	S	05:30:22.18	-43:18:05.3	Y	Y	N	VLA ^u	49	2.580	1.15E-06	2.82E+52	1.1	3.0	46.26, 46.8, [] , 26.[] , []
081126	S, T	21:34:03.59	+48:42:38.3	Y	Y	N	VLA	58	...	3.45E-06	...	6.6	4.4	46.[] , 46.[] , 37.37, []
081203A	S, T	15:32:07.58	+63:31:14.8	Y	Y	N	VLA ^t	223	2.050	7.83E-06	3.47E+53	6.7	21.9	0.3	[1]	2.03	2.17E+50	46.33, 46.33, [] , 26.26, []
081203B	S, T	15:15:11.67	+44:25:42.9	Y	Y	Y	VLA	23	...	2.10E-06	...	58.7	33.7	46.[] , 26.[] , 37.37, []
081221	S, T	01:03:10.20	-24:32:53.2	Y	Y	Y	VLA	34	...	1.89E-05	...	11.4	0.9	46.[] , 46.[] , 26.[] , []
081222	S, T	01:30:57.56	-34:05:41.5	Y	Y	N	VLA	33	2.770	5.22E-06	3.54E+53	25.1	4.9	46.26, 46.23, [] , 26.[] , []
090102	S, T	08:32:58.54	+33:06:51.1	Y	Y	N	VLA ^r	29	1.547	7.06E-06	1.99E+53	23.5	5.0	46.33, 46.33, [] , 26.[] , []
090205	S	14:43:38.65	-27:51:10.7	Y	Y	N	VLA	9	4.650	1.73E-07	2.95E+52	3.4	9.2	46.26, 46.[] , 26.[] , []
090313	S	13:13:36.21	+08:05:49.8	Y	Y	Y	VLA ^r	71	3.375	1.51E-06	4.57E+52	31.9	76.9	0.79	0.6	3.08	6.58E+49	46.33, 46.33, 59.26, []
090323	F	12:42:50.29	+17:03:11.6	Y	Y	Y	VLA ^r	133	3.57	7.32E-05	4.10E+54	28.1	41.2	>20	0.10	>4.63	>1.34E+52	62.63, 46.63, [] , 62.62, 62
090328	F, T	06:02:39.6	-41:53:03.2	Y	Y	Y	VLA	57	0.736	5.40E-05	1.00E+53	61.4	67.4	9	0.26	8.85	1.19E+51	62.63, 46.63, [] , 26.62, 62
090417A ^o	S	02:19:59.00	-07:10:51.0	N	N	N	VLA	0.07	...	2.23E-08	46.[] , 46.[] , 37.37, []
090417B	S	13:58:46.62	+47:01:05.4	Y	N	N	VLA	283	0.345	2.25E-06	1.10E+51	54.5	46.26, 46.[] , 37.37, []
090418	S, T	17:57:15.19	+33:24:21.8	Y	Y	Y	VLA	56	1.608	4.66E-06	2.57E+53	19.0	7.9	46.26, 46.23, [] , 26.[] , []
090423 ^r	S, T	09:55:33.29	+18:08:57.8	Y	Y	Y	VLA	10	8.260	6.25E-07	1.10E+53	5.0	...	>45	0.9	>9.64	>1.66E+51	46.51, 46.33, 59.[] , 2.2
090424	S, T	12:38:05.11	+16:50:15.1	Y	Y	Y	VLA ^{r, v}	50	0.544	2.18E-05	4.47E+52	2.3	35.2	1.6	[1]	6.33	2.73E+50	46.33, 46.33, [] , 33.26, []
090429B	S	14:02:40.05	+32:10:14.3	Y	Y	N	VLA	5.5	9.4	3.10E-07	5.56E+52	0.94	26.64, 26.[] , 37.37, []
090618 ⁿ	S, T	19:35:58.68	+78:21:24.4	Y	Y	Y	VLA ^{r, t}	113	0.540	1.09E-04	2.21E+53	88.8	97.0	0.75	[1]	3.91	5.13E+50	46.12, 46.43, 59.26, 26.[]
090709A	S, T	19:19:42.64	+60:43:39.3	Y	Y	Y	VLA ^r	89	<6.1	2.53E-05	...	85.1	46.26, 46.[] , 59.[] , 26.[]
090715B	S, T	16:45:21.53	+44:50:20.0	Y	Y	Y	VLA	265	3.000	5.67E-06	2.36E+53	8.2	10.8	0.21	[1]	1.39	3.17E+50	46.26, 46.8, 59.26, 26.[]
090809	S	21:54:43.17	-00:05:01.9	Y	Y	N	VLA	8	2.737	3.65E-07	1.39E+52	3.0	5.1	46.26, 46.8, [] , 26.[] , []
090812	S, T	23:32:48.55	-10:36:17.0	Y	Y	Y	VLA	75	2.452	5.73E-06	4.40E+53	12.5	1.8	46.26, 46.26, [] , 26.[] , []
090902B	F	17:39:45.6	+27:19:26.6	Y	Y	Y	VLA ^r	...	1.883	1.38E-04	3.09E+54	47.0	14.7	33.[] , 33.[] , 39.[] , []
091020	S, T	11:42:55.21	+50:58:42.2	Y	Y	Y	VLA	39	1.710	3.80E-06	4.56E+52	19.5	4.6	46.26, 46.8, 59.26, []
091127 ⁿ	S, T	02:26:19.8	-18:57:08.3	Y	Y	N	VLA	7	0.490	8.44E-06	1.41E+52	202.7	150.0	46.26, 46.8, 59.26, []
100413A	S, T	17:44:53.22	+15:50:02.4	Y	Y?	Y	EVLA ^v	191	<3.5	6.20E-06	...	12.6	26.54, 26.[] , 37.37, []
100414A	F, T	12:48:29.96	+08:41:34.9	Y	Y	Y	EVLA ^r	26	1.368	7.74E-05	7.79E+53	143.7	58.5	26.26, 26.[] , 37.37, []
100418A ⁿ	S	17:05:27.18	+11:27:40.1	Y	Y	Y	EVLA ^{r, s, u}	7	0.620	3.40E-07	5.20E+50	10.7	122.1	1.11	[1]	8.43	1.41E+49	26.26, 26.8, [] , 41.26, []
100420	S	19:44:30.63	+55:46:09.3	Y	N	N	EVLA	48	<20	5.70E-07	...	0.8	26.26, 26.[] , 37.37, []
100424A	S	13:57:47.46	+01:32:20.3	Y	Y	N	EVLA	104	<11.0	1.60E-06	...	0.8	6.0	26.26, 26.[] , 37.37, []
100528A	sA, F	20:44:33.92	+27:48:23.8	Y	Y	N	EVLA	25	...	1.71E-05	...	22.3	32.2	26.[] , 37.37, 37.37, []
100805A	S	19:59:30.65	+52:37:40.4	Y	Y	N	EVLA	15	...	5.10E-07	...	6.9	3.7	26.[] , 26.[] , 59.26, []
100814A	S, T	01:29:53.54	-17:59:42.1	Y	Y	Y	EVLA	175	1.44	9.00E-06	5.97E+52	82.0	137.5	

Table 6 — Continued

1	2	3	4	5	6	7	8	9	10	11	12	13	14	15	16	17	18	19
GRB	Inst. ^a	RA J2000	Decl. J2000	X ^b	O ^c	R ^d	Radio Tel	T_{90} s	z	S_{15-150}^e erg cm ⁻²	$E_{iso}^{bol f}$ erg	$F_X^{11hr g}$ CGS	$F_R^{11hr h}$ μ Jy	t_j d	n^i cm ⁻³	θ_j deg.	$E_{true}^{bol j}$ erg	References ^k

Note. —

^a Abbreviations for instruments: A≡*ASM*; B≡*BeppoSAX*; F≡*Fermi*; H≡*HETE*; I≡*INTEGRAL*, P≡*PCA*; S≡*Swift*; sA≡*superAGILE*, T≡*IPN Triangulation*

^b X-ray afterglow. Y≡detection, N≡no detection, Y?≡non-confirmed detection

^c Optical afterglow. Y≡detection, N≡no detection, Y?≡unconfirmed detection

^d Radio afterglow. Y≡detection, N≡no detection, Y?≡unconfirmed detection

^e GRB fluences in 15–150 keV range. For non-*Swift* fluences, the available fluences have been extrapolated to this energy range using formulation of Nysewander et al. (2009).

^f k -corrected bolometric isotropic energy in 1–10,000 KeV range.

^g X-ray flux at 11 hr in 10^{-13} erg cm⁻² s⁻¹. The fluxes are mentioned in 0.3 – 10 keV energy range. However, the fluxes for the *BeppoSAX* bursts are quoted in the energy range of 1.6 – 10 keV.

^h Optical R band flux density at 11 hr in μ Jy.

ⁱ The GRBs for which number densities are not available, we assume number density of 1 cm⁻³. These are denoted as [1].

^j Collimated corrected energy.

^k References are in the following order: T_{90} , z , fluence, bolometric isotropic energy, X-ray flux at 11 hr, Optical flux density at 11 hr, jet break time and density. If a particular cell is empty, then reference has value ‘[]’. However, a reference value ‘[]’ for a non-empty corresponding cell means that we have estimated the values ourselves using GCN circulars. Abbreviations for the references are as follows:

1=(Aleksić et al. 2010); 2=(Chandra et al. 2010); 3=(Amati 2006); 4=(Antonelli et al. 2000); 5=(Berger et al. 2005a); 6=(Berger et al. 2007); 7=(Bloom et al. 2001); 8=(Butler et al. 2007); 9=(Cardone et al. 2009); 10=(Cenko et al. 2006); 11=(Chandra et al. 2008); 12=(Dado & Dar 2010); 13=(de Pasquale et al. 2006); 14=(Firmani et al. 2006); 15=(Frail et al. 2000); 16=(Frail et al. 2001); 17=(Frail et al. 2006); 18=(Frail et al. 2006); 19=(Frontera et al. 2009); 20=(Fynbo et al. 2009); 21=(Gehrels et al. 2008); 22=(Ghirlanda et al. 2004); 23=(Ghirlanda et al. 2010); 24=(Gorosabel et al. 2005); 25=(Graham et al. 2009); 26=http://gcn.gsfc.nasa.gov/gcn3_archive.html; 27=(Hjorth & Bloom 2011); 28=(Connaughton et al. 1997); 29=(Smith et al. 1997b); 30=(Gandolfi et al. 1999); 31=(Jakobsson et al. 2004); 32=(Kann et al. 2011); 33=(Kann et al. 2010); 34=(Kuin et al. 2009); 35=(Lazzati et al. 2001); 36=(Liang et al. 2007); 37=(Nysewander et al. 2009); 38=(Oates et al. 2009); 39=(Pandey et al. 2010); 40=(Pélangeon et al. 2008); 41=(de Ugarte Postigo et al. 2011a); 42=(Racusin et al. 2009); 43=(Rao et al. 2011); 44=(Sakamoto et al. 2005); 45=(Sakamoto et al. 2008); 46=(Sakamoto et al. 2011); 47=(Soderberg et al. 2004); 48=(Soderberg et al. 2005); 49=(Soderberg et al. 2006b); 50=(Soderberg et al. 2006a); 51=(Tanvir et al. 2010a); 52=(Tanvir et al. 2009); 53=(Yonetoku et al. 2004); 54=<http://www.raunvis.hi.is/~pja/GRBsample.html>; 55=http://gcn.gsfc.nasa.gov/integral_grbs.html; 56=<http://www.ssl.berkeley.edu/ipn3/>; 57=<http://www.grbhosts.org/>; 58=<http://space.mit.edu/HETE/Bursts/>; 59=http://www.swift.ac.uk/xrt_curves/; 60=(Bradt et al. 2001); 61=(Bloom et al. 2003); 62=(Cenko et al. 2011); 63=(McBreen et al. 2010); 64=(Cucchiara et al. 2011); 65=(Berger et al. 2003a); 66=(Greiner et al. 2003); 67=(Christensen et al. 2005); 68=(O’Meara et al. 2010); 69=(Chornock et al. 2010); 70=(Tanvir et al. 2010b)

^l Observed with the WSRT, VLBA, Ryle, ATCA and the GMRT in addition to VLA/EVLA

^m Double jet break

ⁿ SN/GRB

^o SHB

^p XRF

^q Galactic Transient?

^r Also observed with the WSRT

^s Also observed with the VLBA

^t Also observed with the Ryle

^u Also observed with the ATCA

^v Also observed with the GMRT